

Aether Scalar Tensor theory confronted with weak lensing data at small accelerations

T. Mistele¹, S. McGaugh², and S. Hossenfelder^{1,3}

¹ Frankfurt Institute for Advanced Studies, Ruth-Moufang-Str. 1, D 60438 Frankfurt am Main, Germany
e-mail: mistele@fias.uni-frankfurt.de

² Department of Astronomy, Case Western Reserve University, 10900 Euclid Avenue, Cleveland, OH 44106, USA

³ Munich Center for Mathematical Philosophy, Ludwig-Maximilians-Universität, Geschwister-Scholl-Platz 1, D-80539 München, Germany

February 23, 2023

ABSTRACT

Context. The recently-proposed Aether Scalar Tensor (AeST) model reproduces both the successes of particle dark matter on cosmological scales and those of Modified Newtonian Dynamics (MOND) on galactic scales. But the AeST model reproduces MOND only up to a certain maximum galactocentric radius. Since MOND is known to fit very well to observations at these scales, this raises the question whether the AeST model comes into tension with data.

Aims. We test whether or not the AeST model is in conflict with observations using a recent analysis of data for weak gravitational lensing.

Methods. We solve the equations of motion of the AeST model, analyze the solutions' behavior, and compare the results to observational data.

Results. The AeST model shows some deviations from MOND at the radii probed by weak gravitational lensing. This creates a tension with the data. To entirely rule out the model, however, a more advanced data analysis as well as an improved theoretical understanding would be necessary.

Key words. galaxies: kinematics and dynamics – gravitational lensing: weak – dark matter – gravitation

1. Introduction

Recently, various models were proposed that combine the successes of Modified Newtonian Dynamics (MOND, [Milgrom 1983b,a,c](#); [Bekenstein & Milgrom 1984](#)) on galactic scales with those of Λ CDM on cosmological scales. Examples are superfluid dark matter (SFDM, [Berezhiani & Khoury 2015](#); [Berezhiani et al. 2018](#)), the Aether Scalar Tensor (AeST) model ([Skordis & Złotnik 2021, 2022](#)), and the neutrino-based model by [Angus \(2009\)](#) (ν HDM). The focus of this present paper is on the AeST model. An accompanying paper will look at SFDM.

The AeST model is a relativistic model that can reproduce MOND in the vicinity of galaxies and fits the fluctuations in the Cosmic Microwave Background as well as the matter power spectrum. In addition, it has a tensor mode that propagates at the speed of light which avoids difficulties matching the observations associated with GW170817 ([Sanders 2018](#); [Boran et al. 2018](#)).

An important ingredient in the AeST model is a so-called ghost condensate ([Arkani-Hamed et al. 2004, 2007](#)). This ghost condensate is the major difference between the action of the AeST model in the static limit and the standard MOND-type action for multifield theories ([Famaey & McGaugh 2012](#)). The ghost condensate has an energy density that acts as an additional source for the gravitational field equations.

The integrated mass of the ghost condensate is generally negligible close to galaxies, where rotation curves are measured. Beyond a few hundred kpc, however, the ghost condensate mass is

no longer negligible compared to the baryonic mass which leads to deviations from MOND.

This is a desired feature for galaxy clusters where observations require accelerations larger than what MOND predicts ([Aguirre et al. 2001](#); [Sanders 2003](#); [Eckert et al. 2022](#)). It may, however, be in conflict with unprecedented recent observations at large radii around galaxies: The analysis of weak-gravitational lensing data from [Brouwer et al. \(2021\)](#) found MOND-like behavior around galaxies up to ~ 1 Mpc. Here, we explore whether this finding is compatible with the AeST model.

Since MOND is known to fit these observations well, we adopt an indirect approach to comparing the AeST model to observations. First, we introduce a method to quantify the deviation of the AeST model from MOND and analyze for which solutions these deviations are minimal. We then compare these optimal solutions – as well as slightly sub-optimal ones – to the observational data.

2. Equations of motion and chemical potential

For galaxies we can use the quasi-static weak-field limit of the AeST model. In this limit, the model can be described by two fields, $\hat{\Phi}$ and φ , whose equations of motion are (at least in the spherically symmetric case that interests us here, see Ap-

pendix A),

$$\Delta\hat{\Phi} = f_G \cdot 4\pi G_N (\rho_b + \rho_c), \quad (1a)$$

$$\nabla \left(\tilde{\mu} \left(\frac{|\nabla\varphi|}{a_0} \right) \nabla\varphi \right) = f_G \cdot 4\pi G_N (\rho_b + \rho_c), \quad (1b)$$

where a_0 is the MOND acceleration scale and f_G is the conversion factor between Newton's gravitational constant G_N and the constant \hat{G} that appears in the Lagrangian (see Appendix A). We use $a_0 = 1.2 \cdot 10^{-10} \text{ m/s}^2$ (Lelli et al. 2017). Both fields are sourced by the baryonic energy density ρ_b and the ghost condensate density ρ_c . The function $\tilde{\mu}$ can be freely chosen in this model and corresponds to an interpolation function of MOND. That is, it determines how the model interpolates between Newtonian gravity at large accelerations and MOND-like gravity at small accelerations. The constant f_G determines how much of the total acceleration (see below) in the Newtonian limit is due to φ and how much due to $\hat{\Phi}$.

In the AeST model, ordinary matter couples to the metric $g_{\mu\nu}$ in the usual way. The metric has the same form as in General Relativity but with the Newtonian potential Φ being a combination of $\hat{\Phi}$ and φ , namely $\Phi \equiv \hat{\Phi} + \varphi$. Thus, the total acceleration felt by matter is $\mathbf{a}_{\text{tot}} \equiv \mathbf{a}_{\hat{\Phi}} + \mathbf{a}_{\varphi} \equiv -\nabla\hat{\Phi} - \nabla\varphi$.

The ghost condensate energy density ρ_c is given by

$$\rho_c = \frac{m^2}{4\pi G_N f_G} \left(\frac{\dot{\varphi}}{Q_0} - \hat{\Phi} - \varphi \right), \quad (2)$$

where m and Q_0 are constants. For cosmology, Skordis & Złotnik (2021) considered non-linear corrections to this. We do not include these here for reasons discussed in Appendix J.

We didn't set $\dot{\varphi} = 0$ in Eq. (2) because any constant $\dot{\varphi} = -\dot{\hat{\Phi}}$ still gives time-independent equations of motion. Indeed, $\dot{\varphi}$ represents the chemical potential of the condensate. To see this, note that the model is shift-symmetric under $\varphi \rightarrow \varphi + \tilde{c}$, $\hat{\Phi} \rightarrow \hat{\Phi} - \tilde{c}$ for any constant \tilde{c} . In general, to describe equilibrium states, one introduces a chemical potential μ for each symmetry by shifting the Hamiltonian H by $H \rightarrow H - \mu Q$ where Q is the conserved quantity associated with the symmetry. In the AeST model and on the level of the Lagrangian, this corresponds to shifting $\varphi \rightarrow \varphi + \mu$ and $\hat{\Phi} \rightarrow \hat{\Phi} - \mu$ (Mistele 2019; Kapusta 1981; Haber & Weldon 1982; Bilic 2008) or equivalently to considering solutions with $\dot{\varphi} = \mu$ and $\hat{\Phi} = -\mu$. (Note that the parameter m was called μ in Skordis & Złotnik (2021). We use μ instead to denote the chemical potential.)

Consequently, the behavior of the AeST model around galaxies depends on the choice of this chemical potential of the ghost condensate. This corresponds to a choice of boundary condition for the combination $\mu/Q_0 - \Phi$ which is a gauge-invariant variable as shown in Skordis & Złotnik (2022). This is an important difference to MOND where ρ_b alone determines the phenomenology around galaxies.

For real galaxies, these chemical potentials are ultimately set by galaxy formation. Since no simulations of non-linear structure formation in the AeST model are available, we treat the chemical potential of each galaxy as a free parameter. In this regard, the AeST model is similar to SFDM. Both models require a choice of chemical potential to make predictions in galaxies (Berezhiani & Houry 2015; Berezhiani et al. 2018; Mistele 2019; Hossenfelder & Mistele 2020; Mistele 2021; Mistele et al. 2022).

We now assume spherical symmetry. Then, solutions have the same form as in MOND, just with the baryonic mass replaced

by an effective mass that includes the condensate mass,

$$M_{\text{eff}}(r) \equiv M_b(r) + M_c(r) \equiv 4\pi \int_0^r dr' r'^2 (\rho_b(r') + \rho_c(r')). \quad (3)$$

Thus, with the Newtonian acceleration a_N in the negative radial direction,

$$a_N(r) \equiv a_b(r) + a_c(r) \equiv \frac{G_N M_b(r)}{r^2} + \frac{G_N M_c(r)}{r^2}, \quad (4)$$

we can write the total acceleration in the negative radial direction a_{tot} as $a_{\text{tot}} = a_N(r) \cdot \nu(|a_N(r)|/a_0)$ where the interpolation function ν is determined by the free function $\tilde{\mu}$ in the AeST model (see Eq. (1)). Unlike in MOND, a_N can be negative because the condensate mass M_c can be negative. We discuss this in more detail below.

For simplicity, we choose the interpolation function such that

$$a_{\text{tot}}(r) = s_{\text{eff}} \cdot \left(|a_N(r)| + \sqrt{a_0 |a_N(r)|} \right), \quad (5)$$

where s_{eff} is the sign of M_{eff} . We recover MOND by leaving out the contributions from the condensate, $M_c = 0$. Thus, when comparing the AeST model to MOND below, we assume the following acceleration for MOND,

$$a_{\text{MOND}}(r) \equiv a_b(r) + \sqrt{a_0 a_b(r)}. \quad (6)$$

This assumes the same interpolation function for MOND and the AeST model.

This interpolation function has the correct limits, namely $a_{\text{MOND}} \rightarrow a_b$ for accelerations much larger than a_0 and $a_{\text{MOND}} \rightarrow \sqrt{a_0 a_b}$ for accelerations much smaller than a_0 . Still, in general, this choice is too simplistic. But it suffices for our purposes because we are only interested in the small-acceleration regime where all interpolation functions give $a_{\text{MOND}} \approx \sqrt{a_0 a_b}$.

The total acceleration a_{tot} in the AeST model does not explicitly depend on f_G and is the sum of $a_{\hat{\Phi}} = f_G a_N$ and $a_{\varphi} = s_{\text{eff}}((1 - f_G)|a_N| + \sqrt{a_0 |a_N|})$. Below, we refer to its MOND-like part $\sqrt{a_0 |a_N|}$ and its Newton-like part a_N , respectively, as

$$a_{\hat{\Phi}} \equiv s_{\text{eff}} |a_N|, \quad a_{\varphi} \equiv s_{\text{eff}} \sqrt{a_0 |a_N|}. \quad (7)$$

In the following we assume point particle baryonic masses for simplicity. This suffices for our purposes, because the details of the baryonic mass distribution don't matter much at the large galactocentric radii we consider. See Appendix D for an approximate analytical solution for this case and Appendix E for how we calculate numerical solutions.

3. Deviations from MOND

The AeST model reproduces MOND so long as the condensate's total mass is small compared to the baryonic mass. This condition is usually fulfilled in the inner parts of galaxies but not far away from the galaxy. Indeed, given a maximum allowed fractional deviation δ from MOND, there is an optimal boundary condition for which the MOND-like behavior extends to a finite maximum radius r_{max} . For all other boundary conditions, deviations from MOND set in earlier. This is illustrated in Fig. 1.

Specifically, we impose the maximum allowed deviation δ as

$$\left| \frac{a_{\varphi}(r)}{\sqrt{a_0 a_b(r)}} - 1 \right| = \left| \frac{s_{\text{eff}} \cdot \sqrt{a_0 |a_N(r)|}}{\sqrt{a_0 a_b(r)}} - 1 \right| \leq \delta. \quad (8)$$

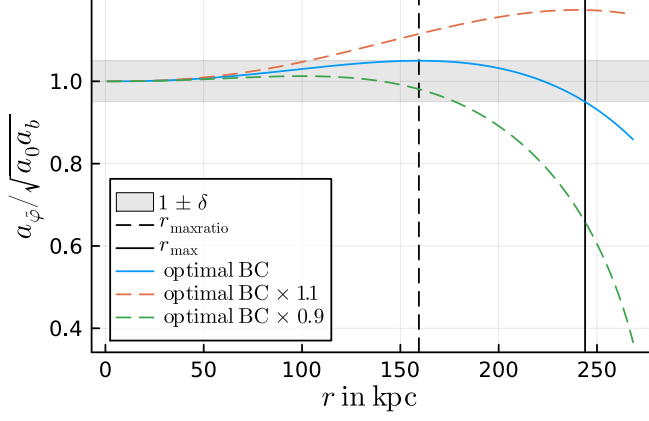


Fig. 1. The numerical solution with the optimal boundary condition for $\delta = 0.05$ (solid blue line). That is, the solution for which $a_{\tilde{\varphi}}$ stays within a fraction δ of the MOND-like acceleration $\sqrt{a_0 a_b}$ up to the maximum possible radius r_{\max} . This is for $M_b = 2 \cdot 10^{10} M_{\odot}$ and $f_G/m^2 = 0.99 \text{ Mpc}^2$. The dashed red and green lines show solutions with the optimal boundary condition multiplied by 1.1 and 0.9, respectively. Vertical black lines indicate the maximum radius r_{\max} and the radius where the optimal solution reaches its maximum $r_{\max\text{ratio}}$.

That is, we compare the accelerations in the AeST model and MOND, focusing on the MOND-like contributions $\sqrt{a_0 a_N}$ and $\sqrt{a_0 a_b}$. Alternatively, we could compare the total acceleration in both models, i.e. $a_N + \sqrt{a_0 a_N}$ and $a_b + \sqrt{a_0 a_b}$. But at the large radii we consider here, the difference is negligible (see Appendix H) and we use Eq. (8) for simplicity.

The maximal radius r_{\max} , up to which we allow accelerations to deviate by less than a fraction δ from MOND, is given by

$$\frac{r_{\max}}{r_{\text{MOND}}} \approx 1.53 \left(9 \frac{(1 + \delta)^2 - 1}{r_{\text{MOND}}^2 m^2 / f_G} \right)^{1/3}. \quad (9)$$

Here, r_{MOND} is a constant known as the MOND-radius $\sqrt{G_N M_b / a_0}$. See Appendix H for a derivation of those properties and an analysis of the conditions under which this estimate holds.

This maximum radius r_{\max} scales as $M_b^{1/6}$. This means that more massive galaxies can stay close to MOND up to larger radii than less massive galaxies. In MOND, however, accelerations $a_b = G_N M_b / r^2$ are more relevant than radii r . For example, the Radial Acceleration Relation (RAR, Lelli et al. 2017) relates the total acceleration a_{tot} and the Newtonian baryonic acceleration a_b .

The maximum radius r_{\max} corresponds to a minimum acceleration $a_{b,\min} = G_N M_b / r_{\max}^2$ which scales as $M_b^{2/3}$. Thus, in acceleration space, less massive galaxies can stay close to MOND for longer than more massive galaxies. We show $a_{b,\min}$ in Fig. 2 and illustrate the RAR for various baryonic masses in Fig. 3.

The scale of r_{\max} is set by the combination m^2 / f_G . Skordis & Złosnik (2021) require $m^2 / f_G \lesssim 1 \text{ Mpc}^{-2}$. As we show below, this does not guarantee MOND-like behavior for weak lensing which probes radii up to $\sim 1 \text{ Mpc}$. One might therefore want to choose an even smaller m^2 / f_G . But this is not easily possible. Indeed, galaxy clusters require more acceleration than MOND predicts (Aguirre et al. 2001; Sanders 2003; Eckert et al. 2022). To naturally explain this in the AeST model, m^2 / f_G cannot be much smaller than 1 Mpc^{-2} and we assume

$$m^2 / f_G \sim (1 \text{ Mpc})^{-2}. \quad (10)$$

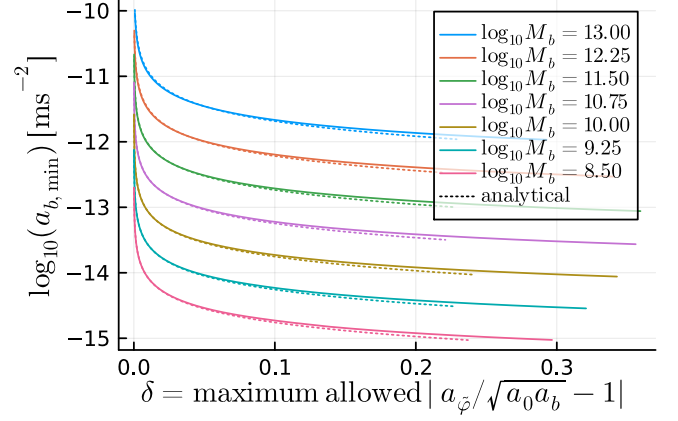


Fig. 2. The acceleration $a_{b,\min} = G_N M_b / r_{\max}^2$ down to which the acceleration $a_{\tilde{\varphi}} = s_{\text{eff}} \sqrt{a_0 |a_N|}$ can, at best, stay within a fraction δ of the MOND-like acceleration $\sqrt{a_0 a_b}$ as a function of δ . This is for $f_G/m^2 = 0.99 \text{ Mpc}^2$. We show the result for both numerical (solid lines) and analytical (dotted lines) solutions and for various baryonic masses M_b . The analytical approximation is shown only where our estimate Eq. (H.8) says that the approximation is better than $q = 10\%$.

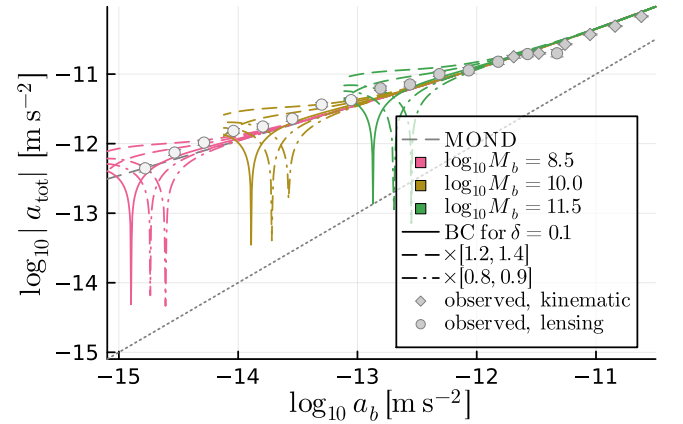


Fig. 3. The RAR for different baryonic masses and boundary conditions for numerical solutions with $f_G/m^2 = 0.99 \text{ Mpc}^2$. The solid lines are for boundary conditions where $a_{\tilde{\varphi}}$ stays within a fraction $\delta = 0.1$ from MOND up to the largest possible radius for a given baryonic mass M_b . Dash-dotted and dashed lines correspond to these optimal boundary conditions multiplied by factors [0.8, 0.9] and [1.2, 1.4], respectively. The dips all go to $-\infty$ since they correspond to $M_{\text{eff}} = 0$, i.e. $a_{\text{tot}} = 0$, but this is not resolved numerically. The y-axis shows the modulus of a_{tot} . So after the dip, the direction of the accelerations is flipped. All solutions are cut off where the condensate density of the largest boundary-condition solution for a given M_b first drops to zero. The observed weak-lensing RAR does not include the hot gas estimate of Brouwer et al. (2021). We correct the observed weak-lensing RAR to be consistent with the M/L_* scale of the observed kinematic RAR (McGaugh 2022, priv. comm.). Data points below $a_b = 10^{-13} \text{ m/s}^2$ have a lighter color since the isolation criterion is less reliable there (Brouwer et al. 2021).

We obtain this estimate by requiring that the minimum acceleration $a_{b,\min}$ in AeST matches where observed clusters deviate from MOND. For example, if we require that the total acceleration a_{tot} in a cluster with $M_b = 10^{14} M_{\odot}$ deviates by at

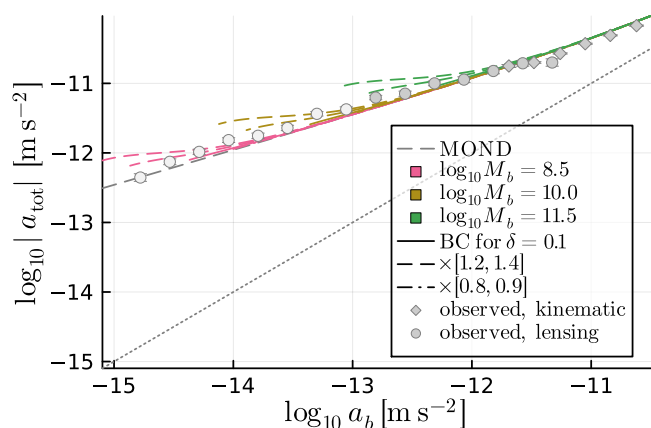


Fig. 4. Same as Fig. 3 but with all solutions truncated where the condensate density first drops to zero, i.e. truncated where the solutions become potentially unstable.

least $\delta = 10\%$ from MOND at $a_{b,\min} = 10^{-10.5} \text{ m/s}^2$, we find $m^2/f_G > 2.5 \text{ Mpc}^{-2}$ (see also Table 1).¹

Beyond the radius where the AeST model deviates from MOND, the gravitational force eventually becomes oscillatory (Skordis & Złosnik 2021), see also Appendix G, as is typical for condensate models (Arkani-Hamed et al. 2007). The reason is that $M_{\text{eff}}(r)$ and the condensate density ρ_c oscillate. However, condensates with negative energy-density are unstable (or at least we would expect a good reason for why they are not unstable). We therefore expect the AeST model to be unstable in this oscillatory regime. We would then no longer have a macroscopically coherent condensate and the quasi-static action Eq. (A.1) is no longer good to use.

In superfluid dark matter models, for example, we assume that when the energy-density begins to oscillate that we have to continue the condensate density by a standard (non-superfluid) phase (Berezhiani & Khoury 2015; Berezhiani et al. 2018). Something similar might happen in the AeST model.

However, so far, a stability analysis for the AeST model in a galactic background has not been done, so maybe the oscillatory regime turns out to be stable after all. Below, we therefore keep in mind both possibilities and discuss where our results depend on whether or not negative condensate densities are stable. For example, Fig. 4 shows the solutions from Fig. 3 but truncated where the condensate density first drops to zero.

But regardless of what happens with the energy-density eventually, when accelerations in AeST begin to deviate from MOND, they generally take on larger values than in MOND because the condensate mass makes an additional contribution. This seems to fit with the fact that dwarf spheroidals tend to fall above the MOND prediction around $a_b \sim 10^{-12} \text{ m/s}^2$ in the observed RAR from Lelli et al. (2017). This could be naturally explained in the AeST model if the minimum acceleration $a_{b,\min}$ was around 10^{-12} m/s^2 for dwarf spheroidals which could be achieved by choosing the model parameter m^2/f_G appropriately.

However, if we do chose $a_{b,\min}$ so that deviations set in around 10^{-12} m/s^2 for dwarf spheroidals, then deviations will set

¹ Here, we did not use the analytical estimate Eq. (9) for r_{\max} when calculating $a_{b,\min} = G_N M_b / r_{\max}^2$. The reason is that Eq. (9) is derived using approximations that are better for galaxies than for clusters. Instead, we calculate r_{\max} from numerical solutions of the equations of motion. Using Eq. (9) would give $m^2/f_G > 7.9 \text{ Mpc}^{-2}$.

Table 1. Rough bounds on m^2/f_G

Bound on m^2/f_G	Description
$\lesssim 1 \text{ Mpc}^{-2}$	Galaxies, weak lensing ($a_b \geq 10^{-13} \text{ m/s}^2$)
$\lesssim 0.001 \text{ Mpc}^{-2}$	Galaxies, weak lensing ($a_b \geq 10^{-15} \text{ m/s}^2$)
$\gtrsim 1 \text{ Mpc}^{-2}$	Galaxy clusters ($a_b \sim 10^{-10.5} \text{ m/s}^2$)

Notes. For the bounds from galaxies, we require that galaxies with $M_b = 10^{11} M_\odot$ can reproduce MOND up to a fraction $\delta = 10\%$ for the accelerations a_b probed by weak lensing, i.e. we require that the minimum acceleration $a_{b,\min}$ is sufficiently small for these galaxies. For the bounds for galaxy clusters, we require that a cluster with $M_b = 10^{14} M_\odot$ cannot reproduce MOND to better than $\delta = 10\%$ at accelerations a_b a bit below the MOND acceleration scale a_0 , i.e. we require that $a_{b,\min}$ is sufficiently large for clusters. The bounds on m^2/f_G scale roughly as $\delta a_{b,\min}^{3/2} / M_b$ for small δ .

in even earlier for more massive galaxies since $a_{b,\min} \propto M_b^{2/3}$. And this is exactly the opposite of what one observes: More massive galaxies follow the MOND prediction very well (Lelli et al. 2017). We therefore conclude that the minimum acceleration $a_{b,\min}$ cannot explain the deviations of the dwarf spheroidals from the kinematically-inferred RAR.

At best, galaxy formation in the AeST model might produce boundary conditions that push dwarf spheroidals – but not other galaxies – to deviate from MOND much earlier than the minimum acceleration $a_{b,\min}$. But it is not clear why that should be the case, at least not with our current theoretical understanding.

4. Weak lensing

Thus, the AeST model usually reproduces MOND at the radii probed by rotation curves because the condensate density M_c is negligible there. This means that probing the effects of the condensate requires a different approach. The option we pursue here is to use the recent weak-lensing analysis of Brouwer et al. (2021) which found that accelerations are MOND-like down to at least $a_b \sim 10^{-13} \text{ m/s}^2$.

In the AeST model, matter is coupled to the fields φ and $\hat{\Phi}$ through the metric $g_{\mu\nu}$. In the weak-field limit, this metric has the same form as in General Relativity (GR), just with the Newtonian potential replaced by $\Phi = \hat{\Phi} + \varphi$. We can therefore use the standard formalism for weak lensing just by taking into account $\Phi = \hat{\Phi} + \varphi$.

Most galaxies in the weak-lensing sample from Brouwer et al. (2021) have baryonic masses between $10^{10} M_\odot$ and $10^{11} M_\odot$. For the AeST model with $f_G/m^2 = 0.99 \text{ Mpc}^2$, Fig. 2 shows that MOND-like behavior up to a few 10% is possible down to $a_b \sim 10^{-13} \text{ m/s}^2$ for those galaxies in the sample with baryonic masses $\sim 10^{10} M_\odot$.

Such $O(10\%)$ deviations may be sufficient to match observations. But it is important to keep in mind that in this regime where deviations from MOND start to become important, the details depend on the precise baryonic masses and boundary conditions of the galaxy sample as well as the precise value of the model parameter m^2/f_G . For example, Fig. 2 shows solutions for boundary conditions that are optimal for reproducing MOND. But there is no reason why galaxy formation should result in such optimal boundary conditions. One would therefore expect deviations of AeST from MOND to generally be larger than in the optimal case we depict.

We can derive a rough upper bound on the model parameter m^2/f_G by requiring that AeST can reproduce MOND in

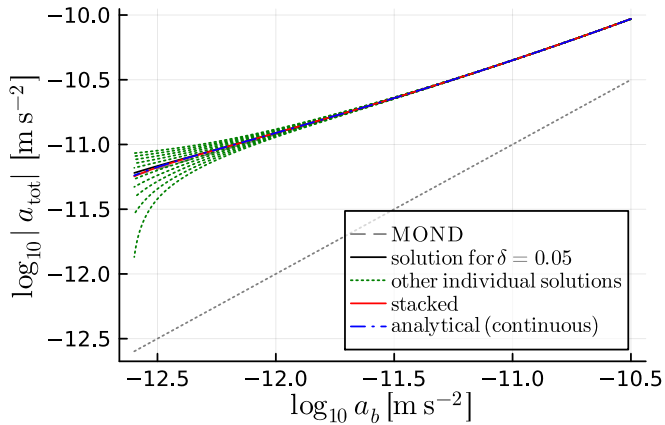


Fig. 5. The RAR for solutions with fixed baryonic mass $M_b = 10^{11} M_\odot$ for various boundary conditions (green dotted lines) and the corresponding stacked RAR (solid red line). This is for $f_G/m^2 = 0.99 \text{ Mpc}^2$. The boundary conditions of the individual solutions are in the range 0.5 – 1.5 times the optimal boundary condition for $\delta = 0.05$ with a step size of 0.1 times the optimal one. Solutions are cut off where the first of the individual solutions reaches $a_{\text{tot}} = 0$. We also show the analytically stacked RAR according to formula Eq. (I.9).

the regime probed by weak lensing. For this, we use the minimum acceleration $a_{b,\text{min}} = G_N M_b / r_{\text{max}}^2$ with r_{max} from Eq. (9). Many of the galaxies in the sample used by Brouwer et al. (2021) have baryonic masses close to $10^{11} M_\odot$. If we require that such galaxies can reproduce MOND down to $a_{b,\text{min}} = 10^{-15} \text{ m/s}^2$ and up to a fraction $\delta = 10\%$, we find $m^2/f_G < 0.001 \text{ Mpc}^{-2}$. There is a lot of uncertainty in this upper bound. For example, $m^2/f_G = 0.001 \text{ Mpc}^{-2}$ is small enough that the ghost condensate density in galaxies as given by Eq. (2) is typically smaller than the cosmological background density. So, at least in principle, there could be corrections from the fact that we should expand around a cosmological background, not around empty Minkowski space (which is how Eq. (1) was derived).² Also, if we disregard the data below $a_b = 10^{-13} \text{ m/s}^2$ because the isolation criterion used in the weak-lensing analysis is less reliable there (Brouwer et al. 2021), we obtain the weaker bound $m^2/f_G < 1 \text{ Mpc}^{-2}$. Still, a tension between the value of m^2/f_G required by weak lensing and that required by galaxy clusters, $m^2/f_G \gtrsim 1 \text{ Mpc}^{-2}$, seems likely (see Table 1).

Another aspect to take into account is that, in practice, the weak-lensing RAR is not known for individual galaxies. It is known only in an averaged sense for a large sample of stacked galaxies. It is possible that stacking gives a MOND-like RAR even if most galaxies individually do not. As we show in Appendix I, in our case, stacking simply means calculating a weighted average in acceleration space. So, indeed, accelerations larger than MOND from some galaxies can cancel accelerations smaller than MOND from other galaxies.

To illustrate this, consider a sample of galaxies with a fixed baryonic mass M_b but various boundary conditions. For simplicity, we weigh all galaxies equally when averaging. One example is shown in Fig. 5. We see how a stacked RAR can be MOND-like even when most individual stacked galaxies are not. Of course, one does not always get a MOND-like RAR from stacking. This works only when accelerations below and above

² But note that there is no reason to expect that such corrections would help to explain why weak-lensing observations follow the MOND prediction down to very small accelerations a_b .

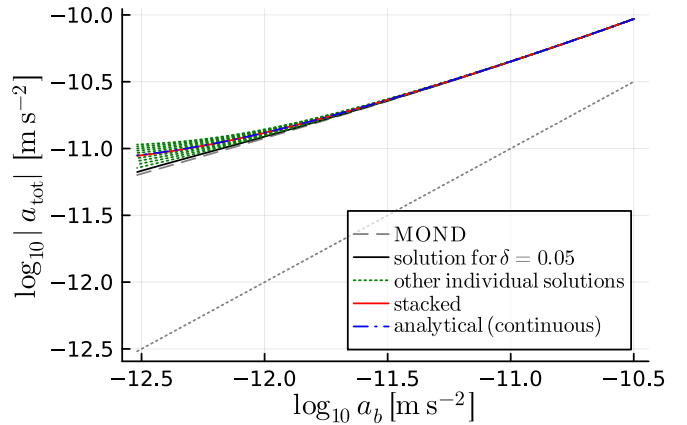


Fig. 6. Same as Fig. 5 but with all individual stacked solutions having positive condensate density. The individual solutions are for boundary conditions in the range 1.0 – 2.0 times the optimal boundary condition for $\delta = 0.05$ with a step size of 0.1 times the optimal one. Solutions are cut off where the first of the individual solutions reaches $\rho_c = 0$.

the MOND prediction cancel each other. Whether or not it works for real lensing galaxies depends on which boundary conditions are picked by galaxy formation.

In addition, stacking galaxies with different boundary conditions should lead to increased uncertainties at small a_b where different boundary conditions lead to significantly different accelerations. In principle, such uncertainties might be visible in the error bars of the observed weak-lensing RAR, but quantifying this is beyond the scope of the present work.

4.1. Negative condensate densities

Whether or not stacked galaxies can follow a MOND RAR down to smaller accelerations than individual galaxies also depends on whether or not negative condensate densities are stable. To see this, note that accelerations are smaller than in MOND if and only if the effective mass $M_{\text{eff}} = M_b + M_c$ is smaller than in MOND. This is only possible for negative M_c which requires negative condensate densities. Therefore, if negative densities are unstable, cancelling accelerations that are larger against those that are smaller than in MOND does not work. Simply because all accelerations are larger than in MOND if we don't allow for negative densities. This is illustrated in Fig. 6.

Thus, if negative densities are unstable, one might expect that the AeST model always gives larger accelerations than MOND. Moreover, our estimate for $a_{b,\text{min}}$ (see Fig. 2) suggests that these deviations should set in earlier for larger baryonic masses M_b . And indeed, there are hints of such behavior in the observed weak-lensing data, see Fig. 7 which shows the weak-lensing data separately for early-type galaxies (ETGs) and late-type galaxies (LTGs). We see that the weak-lensing RAR for LTGs follows the MOND prediction even for $a_b < 10^{-13} \text{ m/s}^2$ while ETGs tend towards larger accelerations than MOND. In general, ETGs have larger baryonic masses than LTGs. So this seems to fit with the AeST model expectations if negative densities are unstable.

However, this M_b -dependence is not a plausible explanation for the difference between the observed weak-lensing RARs for ETGs and LTGs. This is for three reasons.

First, the ETGs and LTGs do not sufficiently differ in baryonic mass. What would be required is a difference in M_b of more than a factor $10^{3/2}$. To see this, note that LTGs follow the MOND

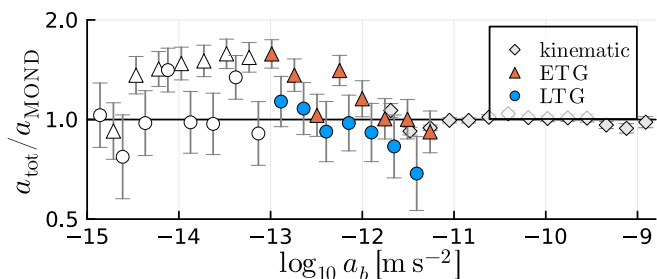


Fig. 7. The observed weak-lensing RAR for ETGs and LTGs from Brouwer et al. (2021) with the stellar M/L_* corrected to use the same stellar population model as the observed kinematic RAR (McGaugh 2022, priv. comm.) relative to the MOND prediction. This does not include the hot gas estimate from Brouwer et al. (2021). Here, we take $a_{\text{MOND}} = a_b v_e(a_b/a_0)$ with $v_e(y) = (1 + e^{-y^5})^{-1}$ (Lelli et al. 2017). Data points below $a_b = 10^{-13} \text{ m/s}^2$ are shown in white since the isolation criterion is less reliable there (Brouwer et al. 2021).

prediction for at least one more order of magnitude in a_b compared to ETGs. This translates into a factor $> 10^{3/2}$ in terms of baryonic mass according to our estimate $a_{b,\text{min}} \propto M_b^{2/3}$. In contrast, Brouwer et al. (2021) selected LTGs and ETGs to have the same stellar mass distribution. With the stellar M/L scale corrected to be consistent with that of the observed kinematic RAR, ETG stellar masses would still be larger by a factor 1.4 (McGaugh 2022, priv. comm.). But this is not sufficient here. Of course, the total baryonic mass should take into account gas, but this does not help here because LTGs contain more gas than ETGs so that the two samples differ by even less than a factor 1.4 in terms of total baryonic mass.

Second, the difference between LTGs and ETGs already has an astrophysically plausible explanation. Namely that the isolation criterion – needed to obtain the weak-lensing RAR – fails first for ETGs since these are more clustered (Dressler 1980).

Third and finally, even if negative densities are indeed unstable, the AeST model does not necessarily predict larger accelerations than MOND. Indeed, it makes no physical sense to stop looking when the condensate becomes unstable. In a real galaxy, something else must follow after the condensate phase. For example, the macroscopically coherent ghost condensate might be replaced by something closer to a Λ CDM-like collisionless fluid which the AeST model postulates on cosmological scales (Skordis & Złosnik 2021). In principle, whatever replaces the ghost condensate might lead to smaller accelerations than MOND.

That said, the prediction of larger-than-MOND accelerations remains valid if whatever replaces the ghost condensate has as its only effect to replace the ghost condensate density by some other positive density, $\rho_c \rightarrow \rho_{\text{replace}}$. This is because then one still has solutions of the same form as before, just with a different effective mass $M_{\text{eff}} \rightarrow M_b + M_{\text{replace}} > M_b$.

In order to get smaller-than-MOND accelerations, the general structure of the solutions must be modified. That is, the left-hand sides of the equations of motions must be modified, $\Delta \hat{\Phi} = \dots, \nabla(\tilde{\mu}(|\nabla\phi|/a_0)\nabla\phi) = \dots \rightarrow ?$. It is not implausible that this indeed happens since the field ϕ plays a role for both the ghost condensate (for example, it carries the chemical potential $\dot{\phi} = \mu$) as well as the gravitational force. So outside the condensate phase both could be modified.

4.2. External Field Effect

Another concern at the small accelerations probed by weak lensing is the External Field Effect (EFE) of MOND (Milgrom 1983b; Famaey & McGaugh 2012). The EFE is a consequence of the specific non-linear form $\nabla(|\nabla\phi|\nabla\phi) \propto \rho_b$ of the gravitational field equations in the small-acceleration limit. The crucial non-linearity is the same in the AeST model, so there’s probably a similar effect there, at least within the ghost condensate.³

The EFE generally reduces the observationally inferred a_{tot} , while a condensate mass $M_c > 0$ in the AeST model enhances this acceleration. In principle, these two effects could cancel each other to give a MOND-like acceleration even at very large galactocentric distances, but there is no reason to expect such a cancellation to generally happen.

And in any case, if negative densities are unstable and the condensate is replaced by something else at large radii, then any potential EFE depends on the details of what replaces the ghost condensate. There could be a modified non-linear effect that still allows neighboring galaxies to affect each other in a way that violates the Strong Equivalence Principle (SEP) like the MOND EFE does. Or there could be no such effect, possibly restoring the SEP at large scales.

A restored SEP would fit with the fact that the observed weak-lensing RAR from Brouwer et al. (2021) shows no signs of an EFE. But here one must be careful. The EFE pertains to non-isolated galaxies, while the analysis of Brouwer et al. (2021) requires isolated galaxies. Thus, any EFE effects may be masked by violations of this assumption. In addition, the environment-dependence of the EFE is quite complicated (Linares et al. 2008; Chae et al. 2021). So it’s not even clear for MOND whether or not a significant EFE is expected here. Still, the EFE is something to keep in mind as observations and theoretical predictions are improved.

5. Conclusion

We have explored whether or not the AeST model can explain the observed MOND-like weak-lensing RAR which probes unprecedentedly small accelerations. We find that deviations from MOND start to set in already in the range of the new measurements, creating a tension with data.

It seems that keeping the model in agreement with data would require specific values of boundary conditions for a large variety of galaxies. While this is possible, we do not know of any mechanism that would result in these particular boundary conditions. More definite results require a more detailed quantitative analysis as well as theoretical advances regarding which boundary conditions are set by galaxy formation and what happens at negative condensate densities.

Acknowledgements. We thank Margot Brouwer for helpful correspondence. This work was supported by the DFG (German Research Foundation) under grant number HO 2601/8-1 together with the joint NSF grant PHY-1911909.

References

- Aguirre, A., Schaye, J., & Quataert, E. 2001, *ApJ*, 561, 550
Angus, G. W. 2009, *Mon. Not. Roy. Astron. Soc.*, 394, 527

³ The EFE is only relevant in situations that are not spherically symmetric. In these cases, as we discuss in Appendix B, the vector field \mathbf{A} of the AeST model cannot be set to zero and the equations of motion are not given by Eq. (1). Still, there is the same type of non-linearity and it is plausible that an effect similar to the MOND EFE exists.

- Arkani-Hamed, N., Cheng, H.-C., Luty, M. A., Mukohyama, S., & Wiseman, T. 2007, *JHEP*, 2007, 036
- Arkani-Hamed, N., Cheng, H. S., Luty, M. A., & Mukohyama, S. 2004, *JHEP*, 2004, 074
- Bekenstein, J. & Milgrom, M. 1984, *ApJ*, 286, 7
- Berezhiani, L., Famaey, B., & Khoury, J. 2018, *JCAP*, 1809, 021
- Berezhiani, L. & Khoury, J. 2015, *Phys. Rev. D*, 92, 103510
- Bilic, N. 2008, *Phys. Rev. D*, 78, 105012
- Boran, S., Desai, S., Kahya, E. O., & Woodard, R. P. 2018, *Phys. Rev. D*, 97, 041501
- Brada, R. & Milgrom, M. 1995, *MNRAS*, 276, 453
- Brouwer, M. M., Oman, K. A., Valentijn, E. A., et al. 2021, *A&A*, 650, A113
- Chae, K.-H., Desmond, H., Lelli, F., McGaugh, S. S., & Schombert, J. M. 2021, *ApJ*, 921, 104
- Dressler, A. 1980, *ApJ*, 236, 351
- Eckert, D., Ettori, S., Pointecouteau, E., van der Burg, R. F. J., & Loubser, S. I. 2022, *A&A*, 662, A123
- Famaey, B. & McGaugh, S. S. 2012, *Living Reviews in Relativity*, 15, 10
- Haber, H. E. & Weldon, H. A. 1982, *Phys. Rev. D*, 25, 502
- Hossenfelder, S. & Mistele, T. 2020, *MNRAS*, 498, 3484
- Ilić, S., Kopp, M., Skordis, C., & Thomas, D. B. 2021, *Phys. Rev. D*, 104, 043520
- Kapusta, J. I. 1981, *Phys. Rev. D*, 24, 426
- Lelli, F., McGaugh, S. S., Schombert, J. M., & Pawłowski, M. S. 2017, *ApJ*, 836, 152
- Llinares, C., Knebe, A., & Zhao, H. 2008, *MNRAS*, 391, 1778
- Milgrom, M. 1983a, *ApJ*, 270, 371
- Milgrom, M. 1983b, *ApJ*, 270, 365
- Milgrom, M. 1983c, *ApJ*, 270, 384
- Milgrom, M. 2021, *Phys. Rev. D*, 103, 044043
- Mistele, T. 2019, *JCAP*, 1911, 039
- Mistele, T. 2021, *JCAP*, 2021, 025
- Mistele, T., McGaugh, S., & Hossenfelder, S. 2022, *A&A*, 664, A40
- Mogensen, P. K. & Riseth, A. N. 2018, *Journal of Open Source Software*, 3, 615
- Rackauckas, C. & Nie, Q. 2017, *Journal of Open Research Software*, 5, 15
- Sanders, R. H. 2003, *MNRAS*, 342, 901
- Sanders, R. H. 2018, *Int. J. Mod. Phys.*, D27, 14
- Skordis, C. & Zlosnik, T. 2021, *Phys. Rev. Lett.*, 127, 161302
- Skordis, C. & Zlosnik, T. 2022, *Phys. Rev. D*, 106, 104041
- Tsitouras, C. 2011, *Computers & Mathematics with Applications*, 62, 770

Appendix A: Action and equations of motion

For galaxies, the quasi-static weak-field limit of the AeST model is relevant. The action in this limit is (Skordis & Złosnik 2021)

$$S = - \int d^4x \left\{ \frac{1}{8\pi\hat{G}} \left[(\nabla\Phi)^2 - 2\nabla\Phi\nabla\varphi + (\nabla\varphi)^2 - m^2 \left(\frac{\dot{\varphi}}{Q_0} - \Phi \right)^2 + \mathcal{J}((\nabla\varphi)^2) \right] + \Phi\rho_b \right\}. \quad (\text{A.1})$$

where \hat{G} is a constant and the function \mathcal{J} determines the MOND interpolation function. We discuss potential higher-order corrections to the m^2 term which produces the ghost condensate density in Appendix J.

The AeST model also contains a unit vector field A^μ . The form Eq. (A.1) of the action assumes $A = 0$ (Skordis & Złosnik 2021). In Appendix B we explain why this assumption is correct in spherical symmetry – which is what we are mainly interested in here – but not in general.

The quasi-static weak-field limit equations of motion derived from the action Eq. (A.1) are

$$\Delta\hat{\Phi} = 4\pi\hat{G}\rho_b + m^2(\mu/Q_0 - \hat{\Phi} - \varphi), \quad (\text{A.2a})$$

$$\nabla \left(\tilde{\mu} \left(\frac{|\nabla\varphi|}{a_0} \right) \nabla\varphi \right) = 4\pi\hat{G}\rho_b + m^2(\mu/Q_0 - \hat{\Phi} - \varphi), \quad (\text{A.2b})$$

where, following Skordis & Złosnik (2021), we have introduced $\hat{\Phi}$ through $\Phi \equiv \hat{\Phi} + \varphi$ and $\tilde{\mu}(|\nabla\varphi|/a_0) = \mathcal{J}'((\nabla\varphi)^2)$. In order to reproduce MOND-like behavior for small accelerations and Newton-like behavior for large accelerations, the function $\tilde{\mu}(|\nabla\varphi|/a_0)$ must be proportional to $|\nabla\varphi|$ for small arguments and it must be a constant for large arguments. As Skordis & Złosnik (2021), we parametrize these limits by a parameter λ_s ,

$$\tilde{\mu} \left(\frac{|\nabla\varphi|}{a_0} \right) \Big|_{|\nabla\varphi| \rightarrow 0} = \frac{\lambda_s}{1 + \lambda_s} \frac{|\nabla\varphi|}{a_0}, \quad \tilde{\mu} \left(\frac{|\nabla\varphi|}{a_0} \right) \Big|_{|\nabla\varphi| \rightarrow \infty} = \lambda_s. \quad (\text{A.3})$$

This ensures both a standard Newton regime at large accelerations and a standard MOND regime at small accelerations with Newtonian gravitational constant

$$G_N \equiv \hat{G} \frac{1 + \lambda_s}{\lambda_s} \equiv \hat{G} \cdot f_G^{-1}. \quad (\text{A.4})$$

How exactly the function $\tilde{\mu}$ interpolates between these two limits is not specified by the AeST model. Various choices are possible. A choice of $\tilde{\mu}$ corresponds to a choice of the so-called interpolation function in MOND (Famaey & McGaugh 2012). Up to the condensate density ρ_c , these equations are typical of multifield MOND models (Famaey & McGaugh 2012).

In the small-acceleration limit $|\nabla\varphi| \ll a_0$ and without any baryonic density, $\rho_b = 0$, these equations approximately become $\nabla(|\nabla\varphi|\nabla\varphi) = c_1 + c_2\varphi$ with constants c_1 and c_2 . This is a special case of the deep-MOND polytropes studied in Milgrom (2021). The results of Milgrom (2021) are not directly useful here, however, because the baryonic density ρ_b plays a very important role for the phenomenology of the AeST model as we will see below.

Appendix B: The quasi-static limit more generally

Had we not set A to zero by hand, the action in the quasi-static limit Eq. (A.1) would read,

$$S = - \int d^4x \left\{ \frac{1}{8\pi\hat{G}} \left[(\nabla\Phi)^2 - 2\nabla\Phi(\nabla\varphi + Q_0A) + (\nabla\varphi + Q_0A)^2 - m^2 \left(\frac{\dot{\varphi}}{Q_0} - \Phi \right)^2 + \mathcal{J}((\nabla\varphi + Q_0A)^2) + \frac{2K_B}{2 - K_B} \nabla_{[i} A_{j]} \nabla^{[i} A^{j]} \right] + \Phi\rho_b \right\}. \quad (\text{B.1})$$

We can decompose A into a divergence-less and a curl-less part, $A \equiv \nabla \times A_c + \nabla A_d$. For time-independent fields – that is, time-independent up to the chemical potential $\dot{\varphi} = \mu = \text{const.}$ – the results of Skordis & Złosnik (2022) show that we can set $A_d = 0$ by a gauge transformation.

In spherical symmetry, the curl term $\nabla \times A_c$ vanishes and the A equation of motion and the φ equation of motion are equivalent. Thus, setting A to zero and using Eq. (A.1) is justified. In general, however, setting A to zero is inconsistent. To see this, consider the A equation of motion,

$$\nabla\Phi + \frac{1}{2Q_0} \frac{2K_B}{2 - K_B} (\Delta A - \nabla(\nabla \cdot A)) = (\nabla\varphi + Q_0A) \left(1 + \mathcal{J}'((\nabla\varphi + Q_0A)^2) \right). \quad (\text{B.2})$$

If A were zero, we could infer

$$\nabla|\nabla\Phi| \times \nabla\Phi = 0, \quad (\text{B.3})$$

by algebraically solving for $\nabla\varphi$ and then taking the curl. But Eq. (B.3) holds only in very special situations, see for example Brada & Milgrom (1995). Thus, except in a few special cases, we must not set $A = 0$ in the quasi-static limit.

Of course, even when Eq. (B.3) does not hold, setting A to zero might still be a reasonable approximation akin to how it is often reasonable to neglect a curl term in standard models of MOND (Famaey & McGaugh 2012). Investigating this is left for future work.

Appendix C: General structure of the solutions

We now assume spherical symmetry. Then, solutions have the same form as in standard multifield MOND models except that the baryonic mass M_b is replaced by the effective mass M_{eff} which includes the condensate mass M_c in addition to M_b . The equations of motion are then solved by

$$a_{\hat{\Phi}} \equiv \hat{\Phi}'(r) = f_G a_N(r), \quad (\text{C.1a})$$

$$a_{\varphi} \equiv \varphi'(r) = a_N(r) \tilde{\nu} \left(\frac{|a_N(r)|}{a_0} \right), \quad (\text{C.1b})$$

where $a_N = G_N M_{\text{eff}}(r)/r^2$ and the function $\tilde{\nu}$ is determined by $\tilde{\mu}$. See e.g. Famaey & McGaugh (2012) for how these two hang together. The total acceleration in the negative radial direction felt by matter is then

$$a_{\text{tot}}(r) = \hat{\Phi}'(r) + \varphi'(r) = a_N(r) \cdot \left(f_G + \tilde{\nu} \left(\frac{|a_N(r)|}{a_0} \right) \right) \equiv a_N(r) \cdot \nu \left(\frac{|a_N(r)|}{a_0} \right), \quad (\text{C.2})$$

where ν is a MOND interpolation function (Famaey & McGaugh 2012).

Below, we are mainly interested in the deep-MOND regime $a_N \ll a_0$. In this regime, the total acceleration does not depend much on the choice of interpolation function. Thus, we choose an interpolation function that is easy to handle,

$$\nu(y) \equiv 1 + 1/\sqrt{y}. \quad (\text{C.3})$$

This interpolation function is not, in general, suited to fit galaxies (Famaey & McGaugh 2012). But it is sufficient in the small-acceleration limit in which we are interested here. This implies for the accelerations due to the field $\hat{\Phi}$ and φ ,

$$\hat{\Phi}'(r) = s_{\text{eff}} \cdot f_G |a_N(r)|, \quad (\text{C.4a})$$

$$\varphi'(r) = s_{\text{eff}} \cdot \left((1 - f_G) |a_N(r)| + \sqrt{a_0 |a_N(r)|} \right), \quad (\text{C.4b})$$

and therefore for the total acceleration

$$\begin{aligned} \hat{\Phi}'(r) + \varphi'(r) &= s_{\text{eff}} \cdot \left(|a_N(r)| + \sqrt{a_0 |a_N(r)|} \right) \\ &= s_{\text{eff}} \cdot \left(\frac{G_N |M_{\text{eff}}(r)|}{r^2} + \frac{\sqrt{a_0 G_N |M_{\text{eff}}(r)|}}{r} \right). \end{aligned} \quad (\text{C.5})$$

For later use, we define

$$\tilde{\Phi}'(r) \equiv s_{\text{eff}} \cdot |a_N(r)| \quad \tilde{\varphi}'(r) \equiv s_{\text{eff}} \cdot \sqrt{a_0 |a_N(r)|} \quad (\text{C.6})$$

That is, $\tilde{\Phi}$ carries the Newton-like part of the total acceleration and $\tilde{\varphi}$ carries the MOND-like part. The total acceleration can be calculated from either $\tilde{\Phi} + \tilde{\varphi}$ or $\hat{\Phi} + \varphi$ since their sum is the same,

$$\hat{\Phi} + \varphi = \tilde{\Phi} + \tilde{\varphi}. \quad (\text{C.7})$$

Appendix D: Approximate analytical solution

The formal solutions Eq. (C.4) are not directly useful since the effective mass M_{eff} in a_N depends on the value of the fields themselves through $\hat{\Phi} + \varphi$. Eq. (C.4) can, however, be used to recursively solve for M_{eff} starting at small radii where the baryonic mass M_b dominates. We first derive the recursion formula and then use it to obtain a 1st order approximation for M_{eff} . For simplicity, we assume a point-particle baryonic mass distribution, $\rho_b(\mathbf{x}) = M_b \delta(\mathbf{x})$.

In the following, we split the fields into a part due only to baryons, i.e. $\hat{\Phi}_b$ and φ_b , and the rest, φ_c and $\hat{\Phi}_c$ which includes the effects of the ghost condensate,

$$\hat{\Phi} \equiv \hat{\Phi}_b + \hat{\Phi}_c, \quad (\text{D.1a})$$

$$\varphi \equiv \varphi_b + \varphi_c, \quad (\text{D.1b})$$

where

$$\hat{\Phi}_b \equiv -f_G \frac{G_N M_b}{r}, \quad (\text{D.2a})$$

$$\varphi_b \equiv -(1 - f_G) \frac{G_N M_b}{r} + \sqrt{G_N a_0 M_b} \ln(r/l), \quad (\text{D.2b})$$

for some l . This split depends on the additive constants chosen for $\hat{\Phi}_b$ and φ_b . In particular, it depends on the choice of l which parametrizes the additive constant in φ_b .

These additive constants can be shuffled around arbitrarily within the physical combination

$$\mu/Q_0 - \hat{\Phi}_b - \hat{\Phi}_c - \varphi_b - \varphi_c. \quad (\text{D.3})$$

To solve the equations of motions, we need to impose a boundary condition for this combination. In practice, we first fix a value of l , i.e. we fix the additive constant in φ_b . Then, it is equivalent to impose a boundary condition for $\mu/Q_0 - \hat{\Phi}_c - \varphi_c$. Here, we choose to impose a value for this combination at $r = 0$,

$$\mu/Q_0 - \hat{\Phi}_c(0) - \varphi_c(0). \quad (\text{D.4})$$

The effective mass M_{eff} is the sum of the baryonic mass M_b and the integrated ghost condensate density ρ_c which depends on the combination $\mu/Q_0 - \varphi - \hat{\Phi}$, see Eq. (2). In turn, Eq. (C.5) allows to calculate the derivative of this combination from M_{eff} . We use this to derive a recursion formula for M_{eff} by equating two different expressions for $\mu/Q_0 - \varphi - \hat{\Phi}$.

In order to get $\mu/Q_0 - \varphi - \hat{\Phi}$ from the derivatives from Eq. (C.5), we must integrate once,

$$\begin{aligned} \mu/Q_0 - \varphi(r) - \hat{\Phi}(r) &= \mu/Q_0 - \varphi_b(r) - \hat{\Phi}_b(r) - \varphi_c(0) - \hat{\Phi}_c(0) \\ &\quad - \int_0^r dr' (\varphi'(r') + \hat{\Phi}'(r') - \varphi_b'(r') - \hat{\Phi}_b'(r')). \end{aligned} \quad (\text{D.5})$$

On the right-hand side, we can plug in Eq. (C.5), i.e. $\varphi' + \hat{\Phi}' = s_{\text{eff}}(G_N |M_{\text{eff}}|/r^2 + \sqrt{a_0 G_N |M_{\text{eff}}|}/r)$, and the same expression but with M_b instead of M_{eff} for $\varphi_b' + \hat{\Phi}_b'$. The left-hand side is proportional to the condensate density ρ_c . Thus, after multiplying by r^2 and integrating once more, the left-hand side is M_{eff} . We find,

$$\begin{aligned} \frac{M_{\text{eff}}(x)}{M_b} &= 1 + \alpha \int_0^x dx' x'^2 \left\{ p_l - \frac{1}{a_0 r_{\text{MOND}}} (\varphi_b(x') + \hat{\Phi}_b(x')) \right. \\ &\quad - \int_0^{x'} dx'' \left[\frac{1}{x''^2} \left(\frac{M_{\text{eff}}(x'')}{M_b} - 1 \right) \right. \\ &\quad \left. \left. + \frac{1}{x''} \left(s_{\text{eff}}(x'') \sqrt{\frac{|M_{\text{eff}}(x'')|}{M_b}} - 1 \right) \right] \right\}, \end{aligned} \quad (\text{D.6})$$

where $r_{\text{MOND}} = \sqrt{G_N M_b / a_0}$ is the MOND radius. We further defined

$$x \equiv \frac{r}{r_{\text{MOND}}}, \quad \alpha \equiv \frac{m^2}{f_G} r_{\text{MOND}}^2, \quad (\text{D.7})$$

and the parameter p_l encodes the boundary condition,

$$p_l \equiv \frac{1}{a_0 r_{\text{MOND}}} \left(\frac{\mu}{Q_0} - \varphi_c(0) - \hat{\Phi}_c(0) \right). \quad (\text{D.8})$$

The subscript l indicates that the split between φ_b , $\hat{\Phi}_b$ and φ_c , $\hat{\Phi}_c$ depends on l .

Eq. (D.6) can be used as a recursion formula to iteratively solve for M_{eff} . The 0th order approximation is to forget about the ghost condensate density, corresponding to $\alpha = 0$, and set

$$M_{\text{eff},0} \equiv M_b. \quad (\text{D.9})$$

The 1st order approximation is obtained from Eq. (D.6) by using the 0th order approximation on the right-hand side, i.e. by setting $M_{\text{eff}} = M_{\text{eff},0} = M_b$ there,

$$\begin{aligned} M_{\text{eff},1}(x) &\equiv M_b \left[1 + \alpha \int_0^x dx' x'^2 \left(p_l - \frac{1}{a_0 r_{\text{MOND}}} (\varphi_b(x') + \hat{\Phi}_b(x')) \right) \right] \\ &= M_b \left[1 + \alpha x^2 \left(\frac{1}{2} + \frac{1}{9} x (3p + 1 - 3 \ln(x)) \right) \right], \end{aligned} \quad (\text{D.10})$$

where

$$p \equiv p_l - \ln\left(\frac{r_{\text{MOND}}}{l}\right) = p_{l=r_{\text{MOND}}}. \quad (\text{D.11})$$

That is, p is the boundary condition for $\mu/Q_0 - \varphi_c - \hat{\Phi}_c$ for the choice $l = r_{\text{MOND}}$.

This 1st order estimate can also be obtained more directly by setting $\varphi = \varphi_b$ and $\hat{\Phi} = \hat{\Phi}_b$ in the ghost condensate density Eq. (2). The advantage of the recursion formula Eq. (D.6) is that it is, at least conceptually, straightforward to improve on this approximation. And it allows to analytically estimate when the 1st order approximation breaks down by going to the next higher order, see Appendix K.5.

In the 1st order approximation, deviations from MOND are proportional to α . This is typically a small number for galaxies. To see this, first note that we typically have $\sqrt{f_G/m} \gtrsim \text{Mpc}$ (Skoldis & Zlosnik 2021). This is much larger than the MOND radius of galaxies, which typically satisfies $r_{\text{MOND}} \lesssim 10 \text{ kpc}$. Thus, α is typically smaller than 10^{-4} for galaxies,

$$\alpha_{\text{galaxies}} = \frac{m^2}{f_G} r_{\text{MOND}}^2 \lesssim 10^{-4} \ll 1. \quad (\text{D.12})$$

In contrast, for galaxy clusters, the MOND radius can be large enough to give $\alpha = \mathcal{O}(1)$.

Appendix E: Numerical solutions

In addition to the analytical approximation discussed above, we also make use of numerical solutions. To obtain these, we use the Julia package ‘OrdinaryDiffEq.jl’ with the ‘AutoTsit5(Rosenbrock23())’ method (Rackauckas & Nie 2017; Tsirtas 2011).

We again use the splits $\hat{\Phi} = \hat{\Phi}_b + \hat{\Phi}_c$ and $\varphi = \varphi_b + \varphi_c$ and numerically solve for $\hat{\Phi}_c$ and φ_c . The equations of motion are

$$\hat{\Phi}_c'' + \frac{2\hat{\Phi}_c'}{r} = S \quad (\text{E.1})$$

$$\frac{\varphi_c'}{r} + \varphi_c'' \frac{1 + F(\varphi_b + \varphi_c)}{2} + \varphi_b'' \frac{F(\varphi_b + \varphi_c) - F(\varphi_b)}{2} = \frac{S}{2\tilde{\mu}(|\varphi_b' + \varphi_c'|/a_0)}, \quad (\text{E.2})$$

where

$$S \equiv m^2 (\mu/Q_0 - \varphi_b - \varphi_c - \hat{\Phi}_b - \hat{\Phi}_c), \quad (\text{E.3})$$

$$\tilde{\mu}(s) = f_G \frac{1 + 2s(1 - f_G) - \sqrt{1 + 4s(1 - f_G)}}{2s(1 - f_G)^2}, \quad (\text{E.4})$$

$$F(\varphi) \equiv \frac{\tilde{\mu}'\left(\frac{|\nabla\varphi|}{a_0}\right) \frac{|\nabla\varphi|}{a_0}}{\tilde{\mu}\left(\frac{|\nabla\varphi|}{a_0}\right)} = \frac{1}{\sqrt{1 + 4(1 - f_G) \frac{|\nabla\varphi|}{a_0}}}. \quad (\text{E.5})$$

On the right-hand side of the φ_c equation, there is in general an additional term proportional to

$$4\pi G_N f_G \rho_b \left(\frac{1}{2\tilde{\mu}(|\varphi_b' + \varphi_c'|/a_0)} - \frac{1}{2\tilde{\mu}(\varphi_b'/a_0)} \right). \quad (\text{E.6})$$

We leave out this term since it vanishes for a baryonic point particle, $\rho_b = M_b \delta(\mathbf{x})$, which is what we consider here. To see that it vanishes, first note that it vanishes outside $r = 0$ because of the factor ρ_b . For $r \rightarrow 0$, we have $\rho_b \propto \delta(r)/r^2$, $\varphi_b' \propto 1/r$, and

$\varphi_c' \propto r$. The behavior of φ_c' can, for example, be read off from our approximate analytical solution which is valid at $r \rightarrow 0$. Thus, we can expand $\tilde{\mu}((\varphi_b' + \varphi_c')/a_0)$ around $\varphi_c' = 0$ and Eq. (E.6) becomes proportional to

$$\rho_b \frac{\tilde{\mu}'(\varphi_b'/a_0)}{\tilde{\mu}(\varphi_b'/a_0)^2} \varphi_c' \rightarrow (1/r^2) \delta(r) (1/r)^{-3/2} \cdot r = \sqrt{r} \delta(r) = 0, \quad (\text{E.7})$$

where we used that $\tilde{\mu}'(s)$ scales as $s^{-3/2}$ at large s while $\tilde{\mu}(s)$ becomes constant.

We use a dimensionless length variable $y = r/l$ with $l = 1 \text{ kpc}$. We solve the equations in terms of v and u , which are obtained from φ_c and $\hat{\Phi}_c$, respectively, by rescaling and absorbing the constant μ/Q_0 ,

$$\mu/Q_0 - \varphi_c - \hat{\Phi}_c \equiv -A(u + v), \quad (\text{E.8})$$

with $A \equiv 10^{-7}$. We use the boundary conditions

$$u'(0) = v'(0) = 0, \quad (\text{E.9})$$

$$u(0) + v(0) = \text{const}. \quad (\text{E.10})$$

The first follows from spherical symmetry, the second corresponds to a choice of chemical potential for the ghost condensate. When comparing the numerical solution to our analytical approximation, the following relation is useful,

$$u(0) + v(0) = -A^{-1} \sqrt{G_N M_b a_0} (p + \ln(r_{\text{MOND}}/l)). \quad (\text{E.11})$$

The logarithm accounts for the fact that p is defined for $l = r_{\text{MOND}}$ while we use $l = 1 \text{ kpc}$ for the numerical solution.

To avoid numerical complications from the $1/r$ factor in the equations of motion, we do not impose these boundary conditions at $r = 0$ but at $r = 10^{-5} \text{ kpc}$, corresponding to $y = 10^{-5}$.

There is an alternative way to obtain numerical solutions. Namely, the recursion formula for M_{eff} Eq. (D.6) is equivalent to

$$\frac{M_{\text{eff}}''(x)}{M_b} - \frac{2}{x} \frac{M_{\text{eff}}'(x)}{M_b} = -\alpha \left[\left(\frac{M_{\text{eff}}(x)}{M_b} \right) + x \left(s_{\text{eff}}(x) \sqrt{\frac{|M_{\text{eff}}(x)|}{M_b}} \right) \right], \quad (\text{E.12})$$

with boundary conditions $M_{\text{eff}}'(0) = 0$ and $M_{\text{eff}}(\epsilon) = M_b + \delta M$ for some $\epsilon > 0$ and δM . This is a single ordinary differential equation (ODE) which we expect to be simpler and faster to solve numerically than the coupled ODEs Eq. (E.1).

Of course, one does not directly obtain solutions for the fields φ and $\hat{\Phi}$ from Eq. (E.12). But here we are mainly interested in accelerations, i.e. derivatives of these fields. And these can easily be obtained from a solution for M_{eff} by using, for example, Eq. (C.5). We nevertheless choose to solve the more complicated coupled ODEs Eq. (E.1). The reason is that these are more independent of our analytical results regarding M_{eff} , thus giving a better cross-check for these analytical results.

Appendix F: Intermediate radii: Deviations from MOND, negative density, boundary condition dependence

The behavior of the function M_{eff} is illustrated in Fig. F.1 which shows the ratio of accelerations in the AeST model with and without including the condensate mass. Since the condensate

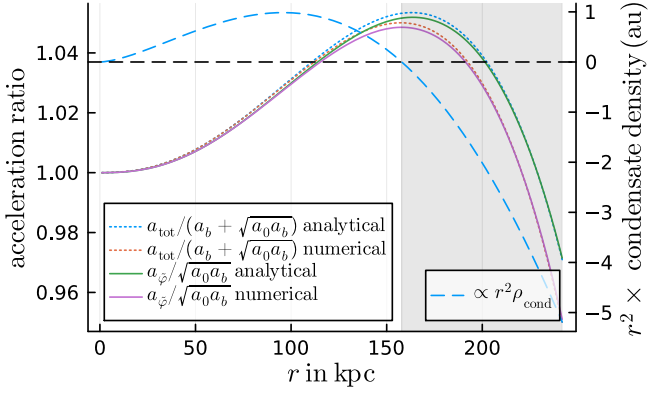


Fig. F.1. Accelerations and condensate density for a galaxy with $M_b = 2 \cdot 10^{10} M_\odot$ and $f_G/m^2 = 0.99 \text{ Mpc}^2$ for both analytical and numerical solutions. Both the numerical and analytical solution use the same boundary condition imposed at $r = 0$ which is chosen such that the maximum of $a_{\text{tot}}/(a_b + \sqrt{a_0 a_b})$ is 1.05 for the numerical solution. In particular, we show the total acceleration a_{tot} relative to the MOND-like acceleration $a_b + \sqrt{a_0 a_b}$ for the analytical (dotted blue line) and numerical (dotted red line) solutions. Similarly, we show the acceleration $a_{\tilde{\varphi}} = \sqrt{a_0 a_b} \sqrt{M_{\text{eff}}/M_b}$ relative to the MOND-like acceleration $\sqrt{a_0 a_b}$ for the analytical (solid green line) and numerical (solid purple line) solutions. The dashed blue line shows r^2 times the ghost condensate density. This density drops to zero where $a_{\tilde{\varphi}}$ has its maximum. At larger radii, the density is negative so the solution is potentially unstable. This is indicated by the shaded region.

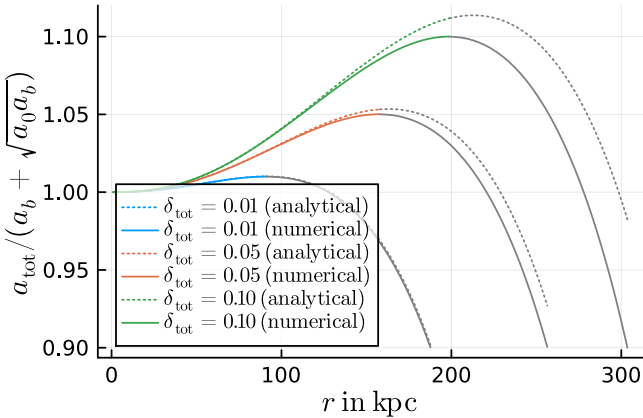


Fig. F.2. The total acceleration a_{tot} relative to the MOND-like acceleration $a_b + \sqrt{a_0 a_b}$ for numerical (solid lines) and analytical (dotted lines) solutions for various boundary conditions for a galaxy with $M_b = 2 \cdot 10^{10} M_\odot$ and $f_G/m^2 = 0.99 \text{ Mpc}^2$. The boundary conditions are chosen such that the maxima of $a_{\text{tot}}/(a_b + \sqrt{a_0 a_b})$ for the numerical solutions are $1 + \delta_{\text{tot}} = 1.01$ (green), 1.05 (red), and 1.10 (blue). For each solution, we indicate the region where the condensate density of the numerical solution is negative with grey line colors.

mass is the only difference to MOND in the limit we consider, this allows to compare the AeST model to MOND.

Among others, Fig. F.1 shows the acceleration $a_{\tilde{\varphi}}$ due to $\tilde{\varphi}'$, i.e. $\sqrt{G_N a_0 M_{\text{eff}}}/r$, relative to what it would be with $M_{\text{eff}} = M_b$, namely $\sqrt{a_0 a_b}$. That is, Fig. F.1 shows,

$$\frac{a_{\tilde{\varphi}}(r)}{\sqrt{a_0 a_b(r)}} = \sqrt{\frac{M_{\text{eff}}(r)}{M_b}}, \quad (\text{F.1})$$

where we assumed $M_{\text{eff}} > 0$. As expected, the condensate mass is small at small radii. There, $M_{\text{eff}}(r) \approx M_b$. At larger radii, the

condensate mass becomes important. In particular, $M_{\text{eff}}(r)$ first reaches a maximum at some finite radius and then drops to zero.

Where and by how much the acceleration in the AeST model differs from MOND depends on the choice of the boundary condition. This is illustrated in Fig. F.2 which shows the total acceleration relative to that in MOND for various boundary conditions. At small radii, all boundary conditions give accelerations close to MOND. At larger radii the boundary-condition-dependent condensate becomes important. This is an important conceptual difference to MOND where the acceleration is fully determined by the baryonic mass distribution.

This qualitative behavior holds not only for the specific numerical values used in Fig. F.1 and Fig. F.2 but more generally. Indeed, this behavior can be read off from our analytical 1st order approximation Eq. (D.10).

The radius where M_{eff} reaches its maximum is the radius where the condensate density drops to zero. This is also illustrated in Fig. F.1. As discussed above, it is plausible that the condensate is unstable for negative densities. So our solutions may not be valid in regions with negative condensate density.

At radii larger than what we show in Fig. F.1, the function M_{eff} begins to oscillate (Skordis & Złotnik 2021). This is not captured by our analytical approximation. We will discuss this more in Appendix G.

Fig. F.1 also shows the ratio of the total acceleration (the sum of both $\tilde{\varphi}'$ and $\tilde{\Phi}'$) relative to what it would be without the condensate mass. We see that this total acceleration is affected by the condensate mass in a similar way as the acceleration $a_{\tilde{\varphi}}$ due to $\tilde{\varphi}'$ alone. This is not surprising: At small radii, M_{eff} is close to M_b so that both $\tilde{\varphi}'$ and $\tilde{\Phi}'$ are not changed significantly by the condensate mass. Thus, also their sum is not changed significantly. At larger radii, M_{eff} deviates from M_b . But there, the acceleration $\tilde{\varphi}'$ dominates. So the sum of $\tilde{\varphi}'$ and $\tilde{\Phi}'$ is close to $\tilde{\varphi}'$.

Fig. F.1 and Fig. F.2 also show both numerical solutions and analytical approximations for the same boundary conditions. The numerical solutions are described in Appendix E. We see that our analytical approximation agrees with the numerical solution quite well. We also see that our approximation is better for smaller δ . We discuss the regime of validity of the analytical approximation in more detail in Appendix H.

Appendix G: Large radii: Oscillations, m^2 - f_G -degeneracy

Above, we saw that the effective mass M_{eff} – and thus also the acceleration – drops to zero at a finite radius. Beyond this radius, the acceleration begins to oscillate (Skordis & Złotnik 2021; Arkani-Hamed et al. 2007), see for example Fig. G.1. As discussed above, this oscillatory regime is potentially unstable since it involved negative energy densities and even negative masses. In this Appendix, we ignore this, keeping in mind that the oscillations might not be physical.

The oscillations depend strongly on the mass parameter m . Larger masses imply shorter oscillation periods and larger amplitudes. Smaller masses imply longer oscillation periods and smaller amplitudes. This is illustrated in Fig. G.1 which shows multiple solutions with the same boundary condition and the same mass M_b but different values of the parameter m . The strong dependence on m is expected as m^2 multiplies the condensate density which is responsible for the deviations from MOND.

More precisely, the condensate density is multiplied by the combination m^2/f_G . Indeed, the total acceleration in the AeST model depends on m^2 and f_G only through this combination

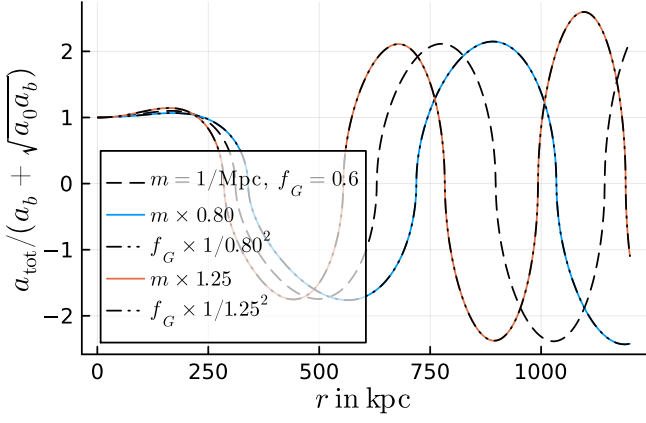


Fig. G.1. The total acceleration a_{tot} relative to the MOND-like acceleration $a_b + \sqrt{a_0 a_b}$ for a galaxy with $M_b = 2 \cdot 10^{10} M_\odot$ for different model parameters m^2 and f_G but with the same boundary condition imposed at $r = 0$. This boundary condition is chosen such that the first maximum of $a_{\text{tot}}/(a_b + \sqrt{a_0 a_b})$ is 1.1 for $m = 1 \text{ Mpc}^{-1}$ and $f_G = 0.6$. This illustrates that the total acceleration begins to oscillate at large radii. It also illustrates that the total acceleration depends only on the combination m^2/f_G but not on m^2 and f_G individually.

m^2/f_G . This is also illustrated in Fig. G.1. Changes in m (such as $m \rightarrow f \cdot m$) give the same solutions as corresponding changes in f_G (namely $f_G \rightarrow f_G/f^2$).

This degeneracy can also be read off directly from the integro-differential equation Eq. (C.5) that determines the total acceleration. The crucial fact is that Eq. (C.5) depends only on the sum $\hat{\Phi} + \varphi$ but not on $\hat{\Phi}$ and φ separately. Individually, $\hat{\Phi}$ and φ do depend on f_G and m^2/f_G separately, see e.g. Eq. (C.4).

Of course, the details of the oscillations depend not only on m^2/f_G but also on the choice of boundary condition and the baryonic mass M_b .

Appendix H: Maximum radius of MOND-like behavior, optimal boundary conditions, relation to maximum of M_{eff}

The AeST model deviates from MOND at large radii. Here, we discuss quantitatively at which radii these deviations occur and how large they are.

First, we point out that deviations from MOND are inevitable. By this we mean that, for given model parameters and a given baryonic mass M_b , one cannot push the deviations to arbitrarily large radii by judiciously adjusting the boundary condition. To see this, consider the effective mass M_{eff} . If deviations from MOND are small, the 0th order approximation $M_{\text{eff},0} = M_b$ should be close to our 1st order approximation $M_{\text{eff},1}$,

$$\frac{M_{\text{eff},1}(r)}{M_b} = 1 + \alpha x^2 \left(\frac{1}{2} + \frac{1}{9} x (3p + 1 - 3 \ln(x)) \right). \quad (\text{H.1})$$

where, again, p parametrizes the boundary condition, $x = r/r_{\text{MOND}}$, and $\alpha = m^2 r_{\text{MOND}}^2 / f_G$. The general form of this function is that it approaches one for $r \rightarrow 0$, has a maximum at some finite radius, and then drops to zero (see e.g. Fig. F.2). This definitely deviates from the 0th order approximation (i.e. from MOND) when it drops to zero. And we can obviously make the radius where this happens arbitrarily large by making the boundary condition p arbitrarily large. So can we avoid deviations from MOND by just making p arbitrarily large? No, because the larger

p is, the more M_{eff} deviates from MOND at its maximum. So there must be a finite optimal boundary condition p . For this optimal boundary condition, the radius up to which deviations from MOND stay small is maximized. We refer to this radius as r_{max} .

More concretely, consider the ratio of the acceleration $a_{\tilde{\varphi}}$ and its value without deviations from MOND, i.e. consider $a_{\tilde{\varphi}} / \sqrt{a_0 a_b}$. Suppose we allow this ratio to deviate from MOND by at most a fraction δ ,

$$\left| \frac{a_{\tilde{\varphi}}(r)}{\sqrt{a_0 a_b(r)}} - 1 \right| = \left| \text{sign}(M_{\text{eff}}(r)) \sqrt{\frac{|M_{\text{eff}}(r)|}{M_b}} - 1 \right| \stackrel{!}{<} \delta. \quad (\text{H.2})$$

That is, suppose we allow $\sqrt{M_{\text{eff}}/M_b}$ to deviate from 1 by at most a fraction δ . Then, there is an optimal boundary condition p that allows this condition to be fulfilled up to a maximum possible radius r_{max} .

As we show in Appendix K.3, this optimal boundary condition is that for which $\sqrt{M_{\text{eff}}/M_b} = a_{\tilde{\varphi}} / \sqrt{a_0 a_b}$ has the value $1 + \delta$ at its maximum. We refer to this radius where $a_{\tilde{\varphi}}$ reaches its maximum as r_{maxratio} . We illustrate the meaning of the quantities r_{max} , r_{maxratio} , and δ in Fig. 1.

As another illustration, consider the solutions in Fig. F.2. These are the optimal solutions for $\delta = 0.01, 0.05$, and 0.10 , respectively. Given the model parameter m^2/f_G and baryonic mass M_b , no other solutions stay within 1%, 5%, and 10% from MOND as long as these. For example, we can read off that, for $M_b = 2 \cdot 10^{10} M_\odot$ and $f_G/m^2 = 0.99 \text{ Mpc}^2$, one can stay within 5% from MOND up to at most about 250 kpc.

Note that the quantity δ is not just relevant when one is interested in optimal solutions given some maximum allowed deviation from MOND. It also provides one way to parametrize the boundary condition, i.e. an alternative to p . All solutions are optimal solutions – just for different values of δ .

Instead of $a_{\tilde{\varphi}}$, we can also consider the total acceleration $a_{\text{tot}} = a_{\tilde{\varphi}} + a_{\tilde{\Phi}}$. This gives an analogous result: If we allow the total acceleration a_{tot} to deviate from MOND by at most a fraction δ_{tot} , then the optimal boundary condition is that for which $a_{\text{tot}}/(a_b + \sqrt{a_0 a_b})$ has the value $1 + \delta_{\text{tot}}$ at its maximum.

Strictly speaking, the optimal boundary conditions for $a_{\tilde{\varphi}} / \sqrt{a_0 a_b}$ and $a_{\text{tot}}/(a_b + \sqrt{a_0 a_b})$ differ. At least for galaxies, however, the optimal boundary conditions are almost identical for both cases. Moreover, the maximizing radius and the value at this maximum are almost identical. This is shown in Appendix K.2. Thus, for our purposes, it doesn't matter much whether we consider the optimal boundary condition for $a_{\tilde{\varphi}}$ or for a_{tot} .

In Fig. H.1 we show the relation between the maximum allowed deviation from MOND δ and the maximum radius r_{max} up to which this condition can be fulfilled. For the numerical solutions, we find r_{max} by maximizing the radius where a solution first deviates by more than a fraction δ from MOND using the Julia package ‘Optim.jl’ (Mogensen & Riseth 2018).

As discussed above, for the optimal boundary conditions, the ratio $a_{\tilde{\varphi}} / \sqrt{a_0 a_b}$ has the value $1 + \delta$ at its first maximum. The radius r_{maxratio} where this maximum occurs is closely related to the radius r_{max} . This is illustrated in Fig. H.2 which shows r_{maxratio} as a function of δ . This is very similar to Fig. H.1 just with the values on the y-axis a bit larger. In particular, r_{maxratio} corresponds to $a_{\tilde{\varphi}} / \sqrt{a_0 a_b} = 1 + \delta$, while r_{max} corresponds to $a_{\tilde{\varphi}} / \sqrt{a_0 a_b} = 1 - \delta$.

We can analytically estimate the relation between δ , r_{max} , and r_{maxratio} , see Appendix K.2. In particular, the maximizer r_{maxratio} is determined by the equation

$$\frac{x^2}{6} + \frac{x^3}{9} \Big|_{x=r_{\text{maxratio}}/r_{\text{MOND}}} = \frac{(1 + \delta)^2 - 1}{\alpha}. \quad (\text{H.3})$$

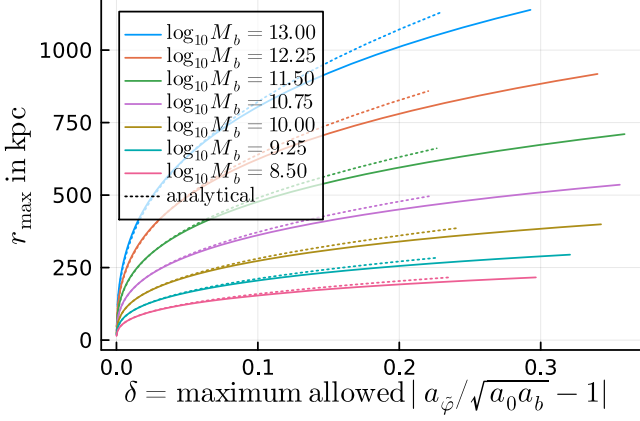


Fig. H.1. The radius r_{\max} up to which the acceleration $a_{\tilde{\varphi}} = \sqrt{a_0 a_b} \sqrt{M_{\text{eff}}/M_b}$ can, at best, stay within a fraction δ of the MOND-like acceleration $\sqrt{a_0 a_b}$ as a function of δ . This corresponds to the radius where $a_{\tilde{\varphi}}/\sqrt{a_0 a_b} = 1 - \delta$ for the optimal boundary condition. This is for $f_G/m^2 = 0.99 \text{ Mpc}^2$. We show the result for both analytical (solid lines) and analytical (dotted lines) solutions and for various baryonic masses M_b . Results for the analytical approximation are shown only where our estimate Eq. (H.8) says that the approximation is better than $q = 10\%$. For the analytical solution we further assume $r_{\max} = 1.53 r_{\text{maxratio}}$ which is valid as long as M_b is not too large.

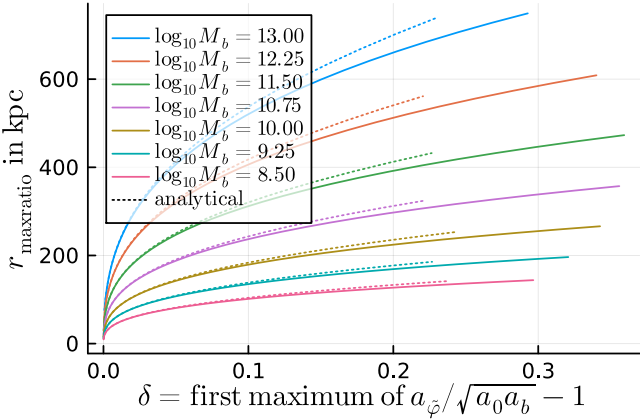


Fig. H.2. The radius r_{maxratio} where the first maximum of the ratio $a_{\tilde{\varphi}}/\sqrt{a_0 a_b}$ occurs for boundary conditions where this maximum deviates from MOND by a fraction δ . These boundary conditions are the optimal boundary conditions given a maximum allowed deviation δ of $a_{\tilde{\varphi}}$ from MOND. This is for $f_G/m^2 = 0.99 \text{ Mpc}^2$. We show the result for both analytical (solid lines) and analytical (dotted lines) solutions and for various baryonic masses M_b . Results for the analytical approximation are shown only where our estimate Eq. (H.8) says that the approximation is better than $q = 10\%$.

This can be solved exactly but the resulting expression is not very illuminating. Qualitatively, when the right-hand side is large, r_{maxratio} is much larger than r_{MOND} . For galaxies, α is typically smaller than 10^{-4} for $m^2/f_G \sim 1/\text{Mpc}^2$. Thus, except for extremely small δ , the right-hand side is indeed large for galaxies. In this case, we have

$$\frac{r_{\text{maxratio}}}{r_{\text{MOND}}} \approx \left(9 \frac{(1+\delta)^2 - 1}{\alpha}\right)^{1/3} - \frac{1}{2} + \mathcal{O}\left(\left(\frac{\alpha}{(1+\delta)^2 - 1}\right)^{1/3}\right). \quad (\text{H.4})$$

To lowest order and using the definition of α , this is

$$\frac{r_{\text{maxratio}}}{r_{\text{MOND}}} \approx \left(9 \frac{(1+\delta)^2 - 1}{r_{\text{MOND}}^2 m^2/f_G}\right)^{1/3}. \quad (\text{H.5})$$

Moreover, we have for galaxies the simple relation

$$r_{\max} \approx 1.53 r_{\text{maxratio}}, \quad (\text{H.6})$$

see Appendix K.4. Thus, at least where this approximation is valid, the only difference between Fig. H.2 and Fig. H.1 is a factor 1.53 in the y-axis values.

Our estimate for r_{\max} can be compared to a related estimate from Skordis & Złotnik (2021). There, the authors estimated that the AeST model acceleration is MOND-like up to a critical radius r_C ,

$$\frac{r_C}{r_{\text{MOND}}} \sim \left(\frac{1}{m^2 r_{\text{MOND}}^2}\right)^{1/3}. \quad (\text{H.7})$$

This has the same scaling in r_{MOND} and m as our estimate. However, our estimate improves on this in a few ways. First, the m^2 factor in r_C should be m^2/f_G . Otherwise, the estimate doesn't correctly take into account the difference between G_N and \hat{G} . Second, our version comes with worked out prefactors, including a parameter that controls how big deviations actually are.

We emphasize again that the maximum radius r_{\max} – or the critical radius r_C – corresponds to choosing boundary conditions that are optimal for reproducing MOND (given an allowed deviation δ). Galaxies are not guaranteed to reproduce MOND up to that radius. In general, galaxies will end up with boundary conditions different from the optimal one and deviate from MOND already at smaller radii.

In Fig. H.1 and Fig. H.2, we show our analytical approximation only where we analytically estimate that it deviates by at most $q = 10\%$ from the full solution. This validity estimate works by going to the next-higher order in our method for approximating M_{eff} and then comparing to our first-order approximation. We find that our first-order approximation of $a_{\tilde{\varphi}}/\sqrt{a_0 a_b}$ deviates from the second order by at most a fraction q up to a radius

$$\frac{r_{\text{approx}}}{r_{\text{maxratio}}} = \frac{1}{2} \left(\beta \delta + \sqrt{(\beta \delta)^2 + 4\beta} \right), \quad (\text{H.8})$$

where

$$\beta = \frac{\sqrt{2}}{3} \sqrt{\frac{1 - (1-q)^2}{\delta^2(2+\delta)}} \sqrt{\frac{(3+2x)^2}{(3+2x)x + 9(2+\delta)}} \Bigg|_{x = \frac{r_{\text{maxratio}}}{r_{\text{MOND}}}}, \quad (\text{H.9})$$

see Appendix K.5. The essential information here is that our approximation is valid for small deviations from MOND δ , but not for larger ones. This can already be guessed from Fig. F.2 and is confirmed here in a more quantitative way.

An important point is that, in order to keep things reasonably simple, we made additional approximations in Appendix K.5. These are valid only up to the maximum r_{maxratio} . Thus, the validity estimate Eq. (H.8) works only up to $r_{\text{approx}} = r_{\text{maxratio}}$. That is, when Eq. (H.8) gives $r_{\text{approx}} < r_{\text{maxratio}}$, our approximation is valid up to this radius r_{approx} to within a fraction q . But a value $r_{\text{approx}} > r_{\text{maxratio}}$ simply means that our approximation is valid up to at least r_{maxratio} . How much larger r_{approx} is compared to r_{maxratio} has no meaning in this case.

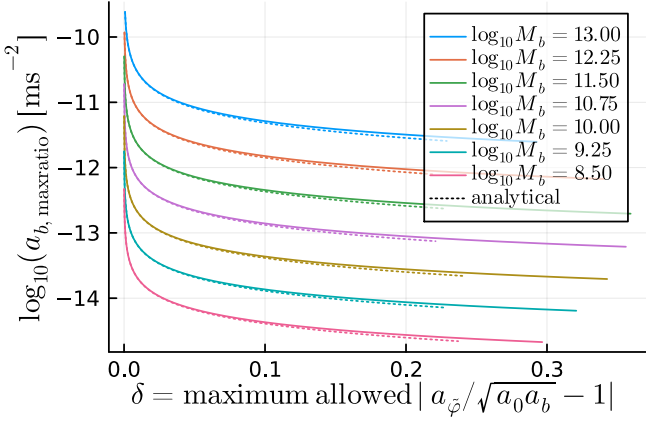


Fig. H.3. Same as Fig. H.2 but in acceleration space rather than position space. That is, the y-axis shows $a_{b,\text{maxratio}} \equiv G_N M_b / r_{\text{maxratio}}^2$ instead of r_{maxratio} .

From Fig. H.1 and Fig. H.2 we see that more massive galaxies can remain close to MOND for longer than less massive galaxies. However, in the context of MOND, accelerations are often more important than radii. Thus, we show the corresponding accelerations $a_{b,\text{min}} = G_N M_b / r_{\text{max}}^2$ and $a_{b,\text{maxratio}} = G_N M_b / r_{\text{maxratio}}^2$ in Fig. 2 and Fig. H.3. We see that the trend is now inverted due to the additional factor of M_b in a_b . Less massive galaxies can have MOND-like behavior down to smaller accelerations than more massive galaxies.

Appendix I: Stacking for weak lensing

In the weak-lensing analysis of Brouwer et al. (2021), the central quantity is the stacked excess surface density (ESD) profile $\Delta\Sigma_{\text{stacked}}$. Stacking here means taking a weighted average over the galaxy sample. More specifically,

$$\Delta\Sigma_{\text{stacked}} = \frac{\sum_i W_i \left(\frac{1}{1+\mu} \epsilon_{t,i} \Sigma_{\text{crit},i} \right)}{\sum_i W_i}, \quad (\text{I.1})$$

where the W_i are weights, Σ_{crit} is the critical surface density, ϵ_t is the ellipticity, and the factor $1 + \mu$ calibrates the shear estimates. The ellipticity ϵ_t of a galaxy is the sum of its intrinsic ellipticity ϵ_t^{int} and the tangential shear γ_t caused by weak lensing. The intrinsic ellipticities average to zero in a large sample, so that $\Delta\Sigma_{\text{stacked}}$ measures the tangential shear γ_t . For an individual lens and up to the calibration factor $1 + \mu$, the combination $\gamma_t \Sigma_{\text{crit}}$ is given by the ESD $\Delta\Sigma$,

$$\Delta\Sigma(R) = \frac{2\pi \int_0^R dR' \Sigma(R')}{\pi R^2} - \Sigma(R), \quad (\text{I.2})$$

where $\Sigma(R)$ is the surface density corresponding to the lensing mass M_{lens} . Thus, for a galaxy sample with known surface densities, we can calculate $\Delta\Sigma_{\text{stacked}}$ by simply averaging the individual ESD profiles of each galaxy,

$$\Delta\Sigma_{\text{stacked}} = \frac{\sum_i W_i \Delta\Sigma_i}{\sum_i W_i}. \quad (\text{I.3})$$

The stacked ESD profile is linear in the surface densities Σ_i . These surface densities are calculated linearly from the density

ρ_{lens} that produces the lensing mass M_{lens} . This lensing mass is defined by $\Phi'(r) = G_N M_{\text{lens}} / r^2$. In our case,

$$\rho_{\text{lens}}(r) = \frac{1}{4\pi G_N r^2} \partial_r \left(r^2 \partial_r (\hat{\Phi} + \varphi) \right). \quad (\text{I.4})$$

Thus, the stacked ESD profile is linear in $\hat{\Phi} + \varphi$. As a consequence, the total acceleration a_{tot} inferred from the stacked ESD profile is just the weighted average of the total accelerations $a_{\text{tot},i}$ of each stacked galaxy,

$$a_{\text{tot,stacked}}(R) = \frac{\sum_i W_i a_{\text{tot},i}(R)}{\sum_i W_i}. \quad (\text{I.5})$$

In order to calculate a stacked RAR, we should not stack at a fixed position R but at a fixed acceleration $a_b = G_N M_b / R^2$. So we should instead use

$$a_{\text{tot,stacked}}(a_b) = \frac{\sum_i W_i a_{\text{tot},i} \left(\sqrt{\frac{G_N M_{b,i}}{a_b}} \right)}{\sum_i W_i}. \quad (\text{I.6})$$

For a fixed baryonic mass M_b , stacking in position space and acceleration space is equivalent.

Let us illustrate how a stacked weak-lensing RAR in the AeST model might look like. For simplicity, we assume that all weights W_i are the same and we further assume that all galaxies have the same baryonic mass M_b . Essentially, we consider stacking a sample of galaxies that differ only in their boundary conditions. Then, we have

$$a_{\text{tot,stacked}}(R) = N^{-1} \sum_i a_{\text{tot},i}(R), \quad (\text{I.7})$$

where N is the number of galaxies in the sample.

Consider now a large number of galaxies with boundary conditions p distributed uniformly in an interval $[p_1, p_2]$. Then, we can write

$$a_{\text{tot,stacked}}(R) = \frac{1}{p_2 - p_1} \int_{p_1}^{p_2} dp a_{\text{tot},p}(R). \quad (\text{I.8})$$

As long as all accelerations $a_{\text{tot},p}(R)$ point in the usual direction, i.e. as long as M_{eff} is positive, this integral can be done analytically for our 1st order analytical approximation,

$$a_{\text{tot,stacked}}(R) \Big|_{M_{\text{eff}} > 0} = a_b \frac{M_{\text{eff}}(x, \bar{p})}{M_b} + \frac{\sqrt{a_0 a_b}}{p_2 - p_1} \frac{2}{\alpha x^3} \left(\left(\frac{M_{\text{eff}}(x, p_2)}{M_b} \right)^{3/2} - \left(\frac{M_{\text{eff}}(x, p_1)}{M_b} \right)^{3/2} \right), \quad (\text{I.9})$$

where $x = r/r_{\text{MOND}}$, $\bar{p} = (p_1 + p_2)/2$, and $M_{\text{eff}}(x, p)$ is our 1st order analytical approximation Eq. (D.10).

Appendix J: Higher-order terms in condensate density

The ghost condensate density from Eq. (2) is linear in the fields φ and $\hat{\Phi}$. In contrast, for their cosmological calculations, Skordis & Zlosnik (2021) used a ghost condensate density including non-linear corrections. Here, we discuss whether using the linearized form around galaxies is valid and explain our decision to do so.

In the full action, not assuming the quasi-static weak-field limit, the condensate density corresponds to a term

$$\mathcal{K}(Q) = \mathcal{K}_2(Q - Q_0)^2, \quad (\text{J.1})$$

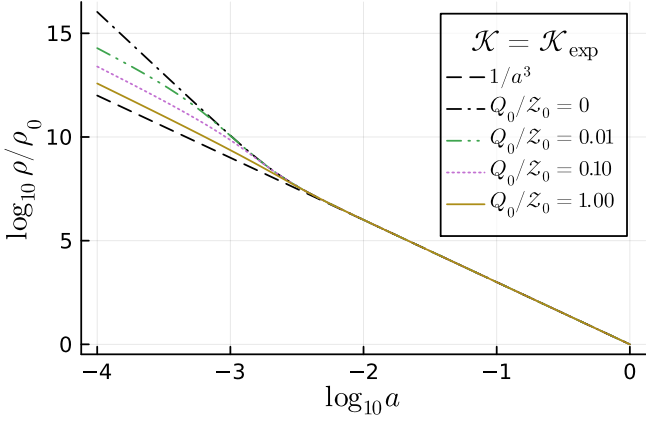


Fig. J.1. The cosmological ghost condensate density ρ as a function of the scale factor a relative to its density ρ_0 today, at $a = 1$, for various values of the combination Q_0/Z_0 . This is for $m = 1 \text{ Mpc}^{-1}$, $K_B = 0.1$, $H_0 = 70 \text{ km s}^{-1} \text{ Mpc}^{-1}$, and $\Omega_0 = 0.25$. The ghost condensate follows a dust-like evolution only at late times. Larger values of m allow for dust-like evolution even at $a = 10^{-4}$ but are in conflict with having MOND-like behavior around galaxies.

where $Q = A^\mu \nabla_\mu \phi$ is a scalar combination of the normalized vector field A^μ and the scalar field ϕ . In the quasi-static weak-field limit, $\phi = Q_0 \cdot t + \varphi$. The constant \mathcal{K}_2 is related to the mass parameter m by $m = \sqrt{2\mathcal{K}_2/(2 - K_B)} Q_0$.

Our expression for the ghost condensate Eq. (2) is linear because the function $\mathcal{K}(Q)$ is quadratic. Indeed, in the quasi-static weak-field limit,

$$Q - Q_0 \approx Q_0 \cdot \left(\frac{\dot{\varphi}}{Q_0} - \varphi - \hat{\Phi} \right). \quad (\text{J.2})$$

However, a quadratic function $\mathcal{K}(Q)$ cannot simultaneously satisfy cosmological constraints and support a MOND-like regime in galaxies (Skordis & Złosnik 2021). In particular, cosmological observations require that the ghost condensate's equation of state w satisfies $w \lesssim 0.02$ at a scale factor $a = 10^{-4}$ (Ilić et al. 2021). But if we assume $m^2/f_G \lesssim 1/\text{Mpc}$ in order to have a MOND-like phenomenology around galaxies, w is too large. Indeed, using $0 < K_B < 2$ and $f_G < 1$, (Skordis & Złosnik 2021)

$$w \approx \frac{3H_0^2 \Omega_0}{2(2 - K_B) f_G (m^2/f_G) a^3} \gtrsim 10^{-8} a^{-3}, \quad (\text{J.3})$$

where H_0 is the Hubble constant and Ω_0 is the matter density parameter today. This is illustrated in Fig. J.1 which shows the cosmological ghost condensate density as a function of the scale factor a for $m = 1 \text{ Mpc}^{-1}$ (see the $Q_0/Z_0 = 0$ line, the parameter Z_0 is discussed below). We see that a dust-like evolution is possible at late times but not around $a \sim 10^{-4}$.

To avoid this problem, Skordis & Złosnik (2021) introduced two alternative forms of $\mathcal{K}(Q)$,

$$\mathcal{K}_{\text{exp}}(Q) = \mathcal{K}_2 Z_0^2 (e^{\mathcal{Z}} - 1), \quad (\text{J.4})$$

$$\mathcal{K}_{\text{cosh}}(Q) = 2\mathcal{K}_2 Z_0^2 (\cosh(\mathcal{Z}) - 1), \quad (\text{J.5})$$

where Z_0 is a constant and

$$\mathcal{Z} \equiv \frac{Q - Q_0}{Z_0}. \quad (\text{J.6})$$

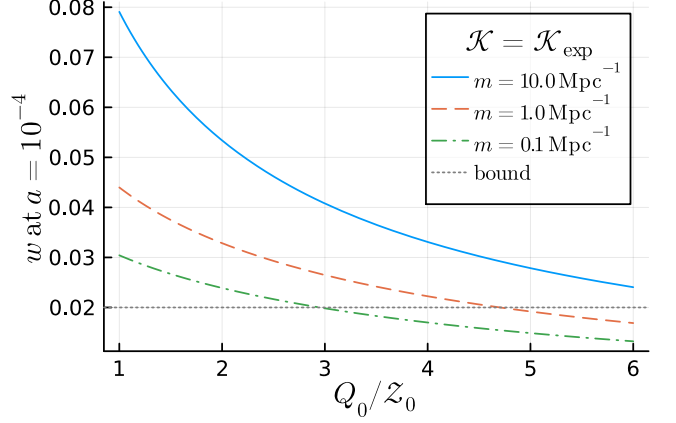


Fig. J.2. Equation of state at $a = 10^{-4}$ as a function of Q_0/Z_0 for the exponential $\mathcal{K}(Q)$ function for various masses m . This is for $K_B = 0.1$, $H_0 = 70 \text{ km s}^{-1} \text{ Mpc}^{-1}$, and $\Omega_0 = 0.25$. The dotted grey line shows the upper bound from Ilić et al. (2021). Note that m^2 is the prefactor of $\mathcal{K}(Q)$. Thus, both the density and the pressure are proportional to m^2 and this prefactor cancels in w . The dependence on m shown here comes from the constraint that the density parameter today is Ω_0 .

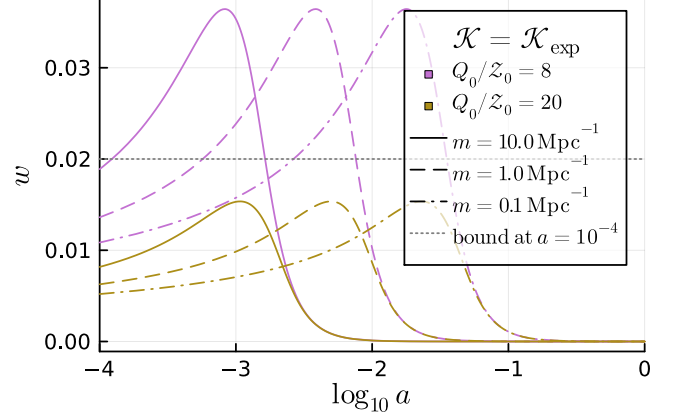


Fig. J.3. Equation of state at w as a function of the scale factor a for the exponential $\mathcal{K}(Q)$ function for various masses m and ratios Q_0/Z_0 . This is for $K_B = 0.1$, $H_0 = 70 \text{ km s}^{-1} \text{ Mpc}^{-1}$, and $\Omega_0 = 0.25$. The dotted grey line shows the upper bound at $a = 10^{-4}$ from Ilić et al. (2021).

These suppress the equation of state at early times where \mathcal{Z} is large and reduce to the quadratic $\mathcal{K}(Q)$ at small \mathcal{Z} .

In our galaxy-scale calculations above, we assumed the quadratic form of $\mathcal{K}(Q)$. This is justified only if \mathcal{Z} is sufficiently small. To see whether or not this is the case, first note that a typical value of $\dot{\varphi}/Q_0 - \varphi - \hat{\Phi}$ around galaxies is 10^{-7} . Thus, a typical value of \mathcal{Z} around galaxies is $\mathcal{Z} \sim \frac{Q_0}{Z_0} \cdot 10^{-7}$. That is, we can use the quadratic $\mathcal{K}(Q)$ as long as

$$\frac{Q_0}{Z_0} \lesssim 10^7. \quad (\text{J.7})$$

Interestingly, this condition is not satisfied, or only barely satisfied, for the explicit cosmological perturbation calculations in Skordis & Złosnik (2021). In particular, Skordis & Złosnik (2021) used $Q_0/Z_0 = 10^8$ for their example calculation using $\mathcal{K}_{\text{cosh}}$ and $Q_0/Z_0 = 10^{13}$ for \mathcal{K}_{exp} .

We nevertheless assume the quadratic form around galaxies for the following reasons. First, this seems to be what the authors

of the model had in mind. After all, they use the quadratic form of $\mathcal{K}(Q)$ when deriving the action for the quasi-static weak-field limit (Skordis & Złosnik 2021).

Second, large values of Q_0/Z_0 do not seem to be required in order to satisfy cosmological constraints. Indeed, the constraint $w \lesssim 0.02$ at $a = 10^{-4}$ can easily be satisfied with a much smaller value of Q_0/Z_0 . This is illustrated for \mathcal{K}_{exp} in Fig. J.2 which shows that $Q_0/Z_0 = \mathcal{O}(1)$ is sufficient.

Even if w satisfies $w \lesssim 0.02$ at $a = 10^{-4}$, it can be larger at later times and potentially violate observational constraints that apply at these later times. Indeed, $w(a)$ is not a monotonous function, as is illustrated in Fig. J.3. Its maximum is set by Q_0/Z_0 and m controls at which scale factor a this maximum occurs. Still, we see from Fig. J.3 that $Q_0/Z_0 = \mathcal{O}(10)$ is sufficient for w to satisfy $w \lesssim 0.02$ even at later times, thus easily satisfying the constraints at these times from Ilić et al. (2021). That is, these constraints can easily be satisfied with $Q_0/Z_0 \ll 10^7$ which allows using the quadratic $\mathcal{K}(Q)$ around galaxies. We find a similar result for $\mathcal{K}_{\text{cosh}}$.⁴

A third reason is that, if the non-linearities of \mathcal{K}_{exp} or $\mathcal{K}_{\text{cosh}}$ were to be important around galaxies, then either many galaxies would deviate very strongly from MOND or there would be almost no deviations from MOND at all. Both cases do not require a thorough investigation here. Strong deviations from MOND are ruled out by observations while pure-MOND predictions are already discussed elsewhere.

It remains to explain why \mathcal{K}_{exp} and $\mathcal{K}_{\text{cosh}}$ have the effects described in the previous paragraph. Consider first \mathcal{K}_{exp} and $\mathcal{K}_{\text{cosh}}$ with the parameter m having roughly the value we assumed above for the quadratic function $\mathcal{K}(Q)$, i.e. $m \sim 1 \text{ Mpc}^{-1}$. Then, as soon as non-linearities become important, the condensate density is enhanced exponentially compared to the case of a quadratic $\mathcal{K}(Q)$. Thus, deviations from MOND set in exponentially earlier, i.e. the radius r_{max} is exponentially smaller. For example, the oscillations discussed in Appendix G start at exponentially smaller radii. This is in conflict with, for example, the observed RAR which is MOND-like as discussed above.

One way out would be to make the prefactor m^2 of \mathcal{K}_{exp} exponentially smaller to keep the ghost condensate from becoming large. Indeed, by choosing m^2 sufficiently small, we can get rid of any significant deviations from MOND around galaxies. The predictions of the AeST model in this case are just those of MOND so don't require a special investigation.

A middle ground would be to make m^2 exponentially smaller, but by just the right amount so that deviations from MOND set in on roughly galactic scales. However, the maximum radius r_{max} would still be exponentially sensitive to the galactic potential $\mu/Q_0 - \varphi - \hat{\Phi}$. Thus, for galaxies with slightly larger $\mu/Q_0 - \varphi - \hat{\Phi}$, deviations from MOND still set in at an exponentially smaller radius compared to the quadratic $\mathcal{K}(Q)$. Galaxies with slightly smaller $\mu/Q_0 - \varphi - \hat{\Phi}$ would perfectly follow the MOND predictions up to exponentially large radii. Thus, a significant fraction of galaxies should still deviate strongly from MOND which is not what is observed.

⁴ Of course, in contrast to Skordis & Złosnik (2021), we did not run a full cosmological perturbations calculation. We only considered the constraint on w from the background cosmology. It's possible that new constraints arise from the CMB or other observations pertaining to cosmological perturbation theory. Here, we assume that this is not the case.

Appendix K: A few useful properties of $M_{\text{eff},1}(r)$

In this appendix, we consider a few properties of the analytical 1st order approximation $M_{\text{eff},1}$ from Eq. (D.10),

$$M_{\text{eff},1}(r) = M_b \left[1 + \alpha x^2 \left(\frac{1}{2} + \frac{1}{9} x (3p + 1 - 3 \ln(x)) \right) \right]. \quad (\text{K.1})$$

We sometimes write M_{eff} instead of $M_{\text{eff},1}$ for brevity.

K.1. Increasing functions of boundary condition

We first show that both $a_{\bar{\varphi}}/\sqrt{a_0 a_b}$ and $a_{\text{tot}}/(a_b + \sqrt{a_0 a_b})$ as well as their spatial derivatives are increasing functions of the boundary condition p . At least as long as M_{eff} is positive. This technical result will be useful in Appendix K.3.

Consider first $a_{\bar{\varphi}}/\sqrt{a_0 a_b} = \sqrt{M_{\text{eff}}/M_b}$ as a function of p . Both $M_{\text{eff}}(r)$ and $M'_{\text{eff}}(r)$ are increasing functions of the boundary condition, i.e. of p , for all r . This follows from α and r being positive. Now consider $\sqrt{M_{\text{eff}}(r)}$ and $\partial_r \sqrt{M_{\text{eff}}(r)}$ for radii where M_{eff} is positive. Then, $\sqrt{M_{\text{eff}}(r)}$ is an increasing function of p everywhere because M_{eff} is,

$$\partial_p \sqrt{M_{\text{eff}}(r)} = \frac{\partial_p M_{\text{eff}}}{2 \sqrt{M_{\text{eff}}(r)}} > 0. \quad (\text{K.2})$$

The same holds for the spatial derivative $\partial_r \sqrt{M_{\text{eff}}(r)}$ but it is a bit harder to see. We find

$$\begin{aligned} \partial_p \partial_x \sqrt{M_{\text{eff}}(r)/M_b} &= \frac{3\alpha x^2 18 + \alpha x^2 (6 + x(3p + 2 - 3 \ln(x)))}{\sqrt{2} (18M_{\text{eff}}(r)/M_b)^{3/2}} \\ &= \frac{3\alpha x^2 9 + \alpha x^2 (\frac{9}{2} + x(3p + 1 - 3 \ln(x))) + 9 + \alpha x^2 ((6 - \frac{9}{2}) + x)}{\sqrt{2} (18M_{\text{eff}}(r)/M_b)^{3/2}} \\ &> \frac{3\alpha x^2}{\sqrt{2}} \frac{9M_{\text{eff}}(r)/M_b}{(18M_{\text{eff}}(r)/M_b)^{3/2}} > 0, \end{aligned} \quad (\text{K.3})$$

which follows because r and M_{eff} are positive.

Consider next, again assuming $M_{\text{eff}} > 0$, the function

$$\frac{a_{\bar{\varphi}} + a_{\bar{\Phi}}}{a_b + \sqrt{a_0 a_b}} = \frac{\frac{M_{\text{eff}}}{M_b} \frac{1}{x} + \sqrt{\frac{M_{\text{eff}}}{M_b}}}{\frac{1}{x} + 1} \equiv \frac{H/x + \sqrt{H}}{1/x + 1}. \quad (\text{K.4})$$

where we defined $H = M_{\text{eff}}/M_b$. Since M_{eff} is an increasing function of the boundary condition p , the same holds for this function. The slope of this function with respect to x is also an increasing function of p , but this is again a bit harder to see. We have

$$\begin{aligned} \partial_p \partial_x \frac{H/x + \sqrt{H}}{1/x + 1} &= x^2 \alpha \frac{2xH(4 + 3x) + 4(3 + 2x)H^{3/2} - x^2(1 + x)\partial_x H}{12(1 + x)^2 H^{3/2}}, \end{aligned} \quad (\text{K.5})$$

where we already inserted the explicit expressions for $\partial_p H$ and $\partial_p \partial_x H$ due to their simple form. It now suffices to show positivity of the following expression,

$$\begin{aligned} 2H(4 + 3x) - x(1 + x)\partial_x H &= 2H(4 + 3x) - x^2(1 + x)\alpha(1 + px - x \ln(x)). \end{aligned} \quad (\text{K.6})$$

In general, this can be negative. However, here it can't due to our assumption that M_{eff} is positive. To see this, first use the definition of H to rewrite $x(p - \ln(x))$ in terms of H ,

$$x(p - \ln(x)) = -\frac{3}{2} - \frac{x}{3} + \frac{3}{\alpha x^2}(H - 1). \quad (\text{K.7})$$

With this, we find

$$\begin{aligned} 2H(4 + 3x) - x(1 + x)\partial_x H \\ = H(5 + 3x) + \frac{1}{6}(1 + x)(18 + 3x^2\alpha + 2x^3\alpha) > 0, \end{aligned} \quad (\text{K.8})$$

which completes the proof.

K.2. Maximum

Consider first the maximum of $a_{\tilde{\varphi}}(r)/\sqrt{a_0 a_b(r)} = \sqrt{M_{\text{eff}}(r)}/M_b$. The maximum of both $M_{\text{eff}}(r)$ and $\sqrt{M_{\text{eff}}(r)}$ is determined by $M'_{\text{eff}}(r) = 0$. This condition can be written as

$$p = \ln(x) - \frac{1}{x}, \quad (\text{K.9})$$

which can be solved in terms of the Lambert W function,

$$x = \frac{1}{W(e^{-p})}. \quad (\text{K.10})$$

Using this condition gives further for the maximum of $\sqrt{M_{\text{eff}}}/M_b$ with value $1 + \delta$,

$$\frac{x^2}{6} + \frac{x^3}{9} = \frac{(1 + \delta)^2 - 1}{\alpha}. \quad (\text{K.11})$$

This can be solved exactly but the resulting expression is not particularly illuminating. The size of the right-hand side determines whether the x^2 or the x^3 term dominates. For large values, the x^3 term dominates, for small values the x^2 term dominates. For large right-hand sides, we have for the maximum

$$x = \left(9 \frac{(1 + \delta)^2 - 1}{\alpha}\right)^{1/3} - \frac{1}{2} + \mathcal{O}\left(\left(\frac{\alpha}{(1 + \delta)^2 - 1}\right)^{1/3}\right). \quad (\text{K.12})$$

The boundary condition needed to obtain such a maximum is

$$p = \frac{1}{3} \ln\left(9 \frac{(1 + \delta)^2 - 1}{\alpha}\right) + \mathcal{O}\left(\left(\frac{\alpha}{(1 + \delta)^2 - 1}\right)^{1/3}\right). \quad (\text{K.13})$$

Consider next the maximum of $a_{\text{tot}}/(a_b + \sqrt{a_0 a_b})$, i.e. the maximum of the function

$$\frac{\frac{M_{\text{eff}}}{M_b} \frac{1}{x} + \sqrt{\frac{M_{\text{eff}}}{M_b}}}{\frac{1}{x} + 1} \equiv \frac{H/x + \sqrt{H}}{1/x + 1}, \quad (\text{K.14})$$

assuming $M_{\text{eff}} > 0$. The maximum of this function is both at a similar location and has a similar value as that of $\sqrt{M_{\text{eff}}}$ – at least for galaxies. We first show that the maximum is at a similar location. To this end, we set the derivative with respect to x to zero, plug in $x + \delta_x$ where x is the maximizer of $\sqrt{M_{\text{eff}}}$, expand to lowest order in δ_x , use $H'(x) = 0$, and solve for δ_x . This gives

$$\frac{\delta_x}{x} = \left(\frac{2x}{1+x} + \frac{x(1+x)(x+2\sqrt{H})H''}{2(\sqrt{H}-1)H}\right)^{-1}. \quad (\text{K.15})$$

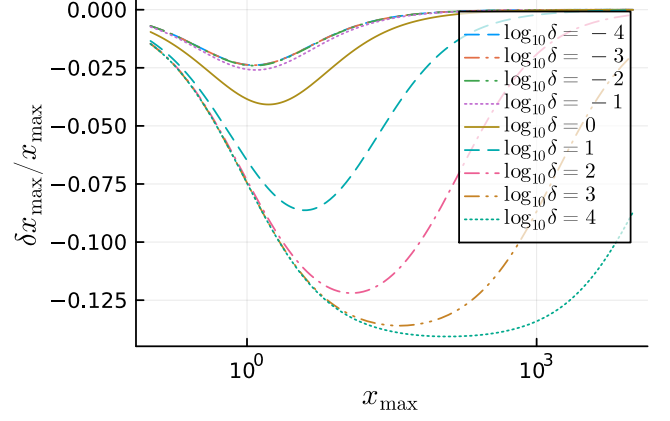


Fig. K.1. The location of the maximum of $a_{\text{tot}}/(a_b + \sqrt{a_0 a_b})$, namely $x_{\text{max}} + \delta x_{\text{max}}$, relative to and as a function of where the maximum of $a_{\tilde{\varphi}}/\sqrt{a_0 a_b}$ lies, namely at x_{max} , for various values of δ according to Eq. (K.16). For clarity, we write x_{max} and δx_{max} instead of x and δ_x .

We have $H(x) = (1 + \delta)^2$ and $H''(x) = -(1 + x)\alpha$ where we used Eq. (K.9). We can further eliminate α by using Eq. (K.11), $\alpha = ((1 + \delta)^2 - 1)/(x^2/6 + x^3/9)$. This gives

$$\frac{\delta_x}{x} = \left(\frac{2x}{1+x} - \frac{9(1+x)^2(2+\delta)(2+x+2\delta)}{x(3+2x)(1+\delta)^2}\right)^{-1}. \quad (\text{K.16})$$

The simplest way to understand this expression is to plot it as a function of x for a number of values of δ , see Fig. K.1. For $\delta \ll 1$, we have that $|\delta_x/x|$ is always smaller than 2.5%. For $\delta = \mathcal{O}(1)$, it can become a bit larger. For example, up to $\delta = 1.5$, we have that $|\delta_x/x|$ is always smaller than 5%. But even for extremely large values of δ , we have that $|\delta_x/x|$ is always smaller than 14.5%. Thus, the maximum of $a_{\text{tot}}/(a_b + \sqrt{a_0 a_b})$ is indeed at a similar location as that of $a_{\tilde{\varphi}}/\sqrt{a_0 a_b}$.

Now we can evaluate the maximum value of the function Eq. (K.14), assuming that the maximizer is close to the one of $\sqrt{M_{\text{eff}}}/M_b$,

$$\frac{\frac{M_{\text{eff}}}{M_b} \frac{1}{x} + \sqrt{\frac{M_{\text{eff}}}{M_b}}}{\frac{1}{x} + 1} \approx \frac{(1 + \delta)^2 + x(1 + \delta)}{1 + x}. \quad (\text{K.17})$$

We can write this as

$$1 + \delta_{\text{tot}} \approx \frac{(1 + \delta_{\tilde{\varphi}})^2 + x(1 + \delta_{\tilde{\varphi}})}{1 + x} = (1 + \delta_{\tilde{\varphi}}) \left(1 + \frac{\delta_{\tilde{\varphi}}}{1 + x}\right), \quad (\text{K.18})$$

where $1 + \delta_{\text{tot}}$ is the maximum value of Eq. (K.14) and $1 + \delta_{\tilde{\varphi}}$ is the maximum of $a_{\tilde{\varphi}}/\sqrt{a_0 a_b}$. Consider first small $\delta_{\tilde{\varphi}}$. Then, the factors relative to MOND are approximately the same in both cases, i.e. $1 + \delta_{\text{tot}} \approx 1 + \delta_{\tilde{\varphi}}$. (But note: δ_{tot} and $\delta_{\tilde{\varphi}}$ themselves might differ by up to a factor 2 for small x). When $\delta_{\tilde{\varphi}}$ is not small, x is very large, see Eq. (K.11). At least for galaxies, which have $\alpha \ll 1$. Thus, the factors relative to MOND are again approximately the same in both cases – unless $\delta_{\tilde{\varphi}}$ is very large. But for such large δ , our approximation is anyway no longer valid, see Appendix K.5.

K.3. Optimal boundary condition

Consider the ratio

$$\frac{a_{\tilde{\varphi}}}{\sqrt{a_0 a_b}} = \sqrt{\frac{M_{\text{eff}}}{M_b}}, \quad (\text{K.19})$$

and require that it stays between $1 + \delta$ and $1 - \delta$ for some positive δ . What is the boundary condition that allows this requirement to be fulfilled up to the maximum possible radius r_{\max} ? We refer to this as the optimal boundary condition. The answer is that it is the boundary condition for which $\sqrt{M_{\text{eff}}/M_b}$ has the value $1 + \delta$ at its maximum, which we discussed in Appendix K.2.

To see this, consider this solution for which $\sqrt{M_{\text{eff}}/M_b}$ has the maximum value $1 + \delta$ at some radius r_1 . This solution will have the value $1 - \delta$ at some radius $r_2 > r_1$ since M_{eff} drops to zero after the maximum. Let this solution's boundary condition p be p_1 .

Here, we consider $M_{\text{eff}} > 0$. When $M_{\text{eff}} < 0$, the gravitational force in the AeST model points into the opposite direction from that in MOND. We are not interested in this regime here. Thus, we assume $\delta < 1$ which implies $M_{\text{eff}} > 0$.

Any solution with a boundary condition p larger than p_1 has a larger value $\sqrt{M_{\text{eff}}}$ everywhere (see Appendix K.1). This implies that such solutions must have $\sqrt{M_{\text{eff}}/M_b} > 1 + \delta$ at $r = r_1$. Thus, boundary conditions p larger than p_1 cannot be optimal.

Consider then solutions with boundary condition p smaller than p_1 . Such solutions have a smaller value $\sqrt{M_{\text{eff}}}$ and slope $\partial_r \sqrt{M_{\text{eff}}}$ everywhere (see Appendix K.1). Thus, these solutions reach their maximum earlier than r_1 and this maximum has a value smaller than $1 + \delta$. Starting at this lower maximum, such solutions then go to zero faster (since their slope is more negative). Thus, these solutions reach $\sqrt{M_{\text{eff}}/M_b} = 1 - \delta$ earlier than r_2 . Thus, smaller boundary conditions also cannot be optimal.

It follows that the optimal boundary condition is that which gives $\sqrt{M_{\text{eff}}/M_b} = 1 + \delta$ at the maximum of M_{eff} , i.e. $p = p_1$.

The preceding argument implicitly considered negative condensate densities by considering radii beyond the radius where M_{eff} is maximal. Does anything change when we restrict solutions to positive densities? The answer is no, at least as long as we just cut off the solutions when the density reaches zero and don't continue them with something else (like e.g. an NFW halo). The above argument can be straightforwardly adapted to this case.

Instead of $a_{\tilde{\varphi}}/\sqrt{a_0 a_b}$ we could also consider the total acceleration relative to MOND, i.e.

$$\frac{a_{\tilde{\varphi}} + a_{\tilde{\Phi}}}{a_b + \sqrt{a_0 a_b}} = \frac{\frac{M_{\text{eff}}}{M_b} \frac{1}{x} + \sqrt{\frac{M_{\text{eff}}}{M_b}}}{\frac{1}{x} + 1}. \quad (\text{K.20})$$

The argument above can be adapted to this case as well. That is, the optimal boundary condition is that for which this total acceleration ratio has the maximum value $1 + \delta$.

The optimal boundary conditions for $a_{\tilde{\varphi}}$ are, in general, not the same as those for the total acceleration $a_{\tilde{\varphi}} + a_{\tilde{\Phi}}$. However, in practice, they are very similar and give very similar deviations from MOND at very similar maximum radius. This follows from the properties of the maximum discussed in Appendix K.2.

K.4. Relation between r_{\max} and r_{maxratio}

Consider a solution that is optimal for some δ . As discussed above and as illustrated in Fig. 1, the radius r_{maxratio} is where the ratio $a_{\tilde{\varphi}}/\sqrt{a_0 a_b}$ has its maximum value, namely $1 + \delta$, and r_{\max} is the radius where this ratio drops to $1 - \delta$. Here, we consider the relation between these two radii. We will argue that, usually, r_{\max} is larger than r_{maxratio} by a fixed factor 1.53 for small δ .

Based on numerical examples, we first guess a factor around 1.5. Then, we calculate first-order corrections to this factor 1.5

and find that corrections are, in a certain regime, small. This confirms the validity of our initial guess. In addition, we find that the first-order corrections are universal and give a factor 1.53.

To find r_{\max} , we must solve $\sqrt{M_{\text{eff}}/M_b} = 1 - \delta$. That is,

$$1 + \alpha x^2 \left(\frac{1}{2} + \frac{1}{9} x(3p + 1 - 3 \ln(x)) \right) = (1 - \delta)^2. \quad (\text{K.21})$$

where $x = r_{\max}/r_{\text{MOND}}$. We write

$$x = f x_0 (1 + \epsilon), \quad (\text{K.22})$$

where x_0 is the radius where this equation is satisfied with $(1 + \delta)$ instead of $(1 - \delta)$ on the right-hand side, i.e. it's the radius where M_{eff} is maximal, that is $x_0 = r_{\text{maxratio}}/r_{\text{MOND}}$. We later set $f = 3/2$ and let ϵ parametrize deviations from a factor 1.5 between r_{\max} and r_{maxratio} , i.e. later we will find $f(1 + \epsilon) \approx 1.53$.

We plug this expression for x back into the equation determining x , expand in ϵ , and solve for ϵ . Then, we eliminate first p and then α using the two conditions we know from x_0 being a maximum, namely Eq. (K.9) and Eq. (K.11). This gives

$$\epsilon = -\frac{1}{3} + \frac{(2 - \delta)(3 + 2x_0) + 3f^2(2 + \delta) + 2f^3 x_0(2 + \delta)}{18f^2(2 + \delta)(f - 1 + f x_0 \ln(f))}. \quad (\text{K.23})$$

This is a function of x_0 of the form $(A + Bx_0)/(C + Dx_0)$. It is monotonically increasing or decreasing depending on the sign of $BC - AD$. The value at $x_0 = 0$ is A/C . For $x_0 \rightarrow \infty$, the value is B/D . So it monotonically interpolates between A/C at small x_0 and B/D at large x_0 .

We now consider $f = 3/2$ and check whether or not ϵ is actually small,

$$\epsilon_{f=3/2} = \frac{12(2 - \delta) + x_0(70 + 19\delta - 81(2 + \delta)\ln(3/2))}{81(2 + \delta)(1 + 3x_0 \ln(3/2))}. \quad (\text{K.24})$$

For large x_0 , this gives

$$\epsilon_{f=3/2} = \frac{70 + 19\delta - 81(2 + \delta)\ln(3/2)}{243(2 + \delta)\ln(3/2)} + \mathcal{O}(1/x_0). \quad (\text{K.25})$$

The maximum radius x_0 is large as long as $\delta/\alpha \gg 1$, see Appendix K.2. For galaxies, we typically have $\alpha \lesssim 10^{-4}$ (see Appendix H). Thus, this condition is fulfilled unless δ is extremely large. For such large δ , the 1st order analytical approximation for M_{eff} is anyway no longer valid, as we show in Appendix K.5. Thus, for galaxies, the large- x_0 result is typically valid.

If, in addition, we have $\delta \ll 1$, we find

$$\epsilon_{f=3/2} = -\frac{1}{3} + \frac{35}{243 \ln(3/2)} + \mathcal{O}(\delta) + \mathcal{O}(1/x_0). \quad (\text{K.26})$$

Thus,

$$\frac{r_{\max}}{r_{\text{maxratio}}} = \frac{3}{2}(1 + \epsilon_{f=3/2}) \approx 1 + \frac{35}{162 \ln(3/2)} \approx 1.53. \quad (\text{K.27})$$

K.5. Validity of approximation

We now consider the validity of our 1st order approximation $M_{\text{eff},1}$ for M_{eff} from Eq. (D.10). Fig. F.2 and other plots suggest that it is often a reasonable approximation but also that it becomes worse for larger deviations from MOND δ . Here, we estimate analytically when this approximation is valid.

To this end, we calculate the 2nd order approximation to M_{eff} and check when the 1st and 2nd orders deviate from each other.

To facilitate a quantitative analytical estimate, we do not calculate the 2nd order approximation exactly. We make additional approximations and assumptions. The result should still be a reasonable estimate of when the 1st order approximation is valid.

The 2nd order approximation is obtained by plugging the 1st order approximation into the right-hand side of Eq. (D.6),

$$\frac{M_{\text{eff},2}(x)}{M_b} = \frac{M_{\text{eff},1}(x)}{M_b} - \alpha \int_0^x dx' x'^2 \int_0^{x'} dx'' \left[\frac{1}{x''^2} \left(\frac{M_{\text{eff},1}(x'')}{M_b} - 1 \right) + \frac{1}{x''} \left(s_{\text{eff},1}(x'') \sqrt{\frac{|M_{\text{eff},1}(x'')|}{M_b}} - 1 \right) \right], \quad (\text{K.28})$$

where the subscripts 1 and 2 refer to the 1st and 2nd order approximations, respectively.

The double integrals in this expression can be done analytically for the part linear in $M_{\text{eff},1}$. We find

$$\frac{M_{\text{eff},2}^{\text{lin}}(x)}{M_b} = \frac{M_{\text{eff},1}(x)}{M_b} - \frac{x^4 \alpha^2}{1800} (225 + (62 + 60p)x - 60x \ln(x)). \quad (\text{K.29})$$

Below we express radii relative to where $M_{\text{eff},1}$ has its maximum,

$$\hat{x} \equiv \frac{r}{r_{\text{maxratio}}} \equiv \frac{x}{x_{\text{mr}}}. \quad (\text{K.30})$$

We can also eliminate p by using the relation $p = \ln(x_{\text{mr}}) - 1/x_{\text{mr}}$. This gives

$$\frac{M_{\text{eff},2}^{\text{lin}}(\hat{x})}{M_b} \approx \frac{M_{\text{eff},1}(\hat{x})}{M_b} - \frac{\hat{x}^4 x_{\text{mr}}^4 \alpha^2}{1800} \left(225 - 60\hat{x} + 62x_{\text{mr}}\hat{x} \left(1 - \frac{60}{62} \ln(\hat{x}) \right) \right). \quad (\text{K.31})$$

Consider \hat{x} between 0 and 1. The function $\hat{x}(1 - 60/62 \ln(\hat{x}))$ grows from 0 to 1 in this \hat{x} interval. Thus, when x_{mr} is large, i.e. when r_{maxratio} is large compared to r_{MOND} , this term will dominate, except at very small radii \hat{x} . Otherwise, the $225 - 60\hat{x}$ term dominates.

We now consider the remaining terms in $M_{\text{eff},2}/M_b$, i.e. those with $\sqrt{M_{\text{eff},1}/M_b}$. Here, the double integrals are not straightforward to do analytically. Therefore, we make an additional approximation and we restrict ourselves to radii r before $M_{\text{eff},1}$ reaches its maximum, i.e. we only consider $r \leq r_{\text{maxratio}}$. Concretely, we assume that $\sqrt{M_{\text{eff},1}/M_b} = a_{\hat{\varphi},1}/\sqrt{a_0 a_b}$ grows linearly from 1 at $r = 0$ to its maximum $1 + \delta$ at $r = r_{\text{maxratio}}$,

$$\frac{a_{\hat{\varphi},1}(r)}{\sqrt{a_0 a_b(r)}} = \sqrt{\frac{M_{\text{eff},1}(r)}{M_b}} = 1 + \delta \frac{r}{r_{\text{maxratio}}}, \quad r \leq r_{\text{maxratio}}. \quad (\text{K.32})$$

From Fig. 1 and Fig. F.1 we see that this underestimates $M_{\text{eff},1}$ at small radii and then overestimates it at larger radii towards r_{maxratio} . This is a rough approximation but we have verified numerically that it captures the validity of the 1st order approximation reasonably well. With this, we have

$$\frac{M_{\text{eff},2}^{\text{sqrt}}(x)}{M_b} = -\frac{\alpha \delta}{4} x_{\text{mr}}^3 x^4. \quad (\text{K.33})$$

The remaining task is to sum $M_{\text{eff},2}^{\text{lin}}$ and $M_{\text{eff},2}^{\text{sqrt}}$ and determine when this sum deviates from $M_{\text{eff},1}$. More specifically, we are interested mostly in $a_{\hat{\varphi}}$ so we are interested in the square root. We parametrize the deviation by a parameter q ,

$$\sqrt{\frac{M_{\text{eff},2}(\hat{x})}{M_{\text{eff},1}(\hat{x})}} \stackrel{!}{=} 1 - q. \quad (\text{K.34})$$

This relation determines the radius \hat{x} where the 2nd order becomes important if we want to trust the 1st order approximation up to a fraction q .

Unfortunately, this equation is not straightforward to solve analytically. Thus, we make further approximations. First, we use the linear approximation $\sqrt{M_{\text{eff},1}/M_b} = 1 + \delta \hat{x}$ also in the denominator of Eq. (K.34) and the first term in $M_{\text{eff},2}^{\text{lin}}$. Second, we neglect the $\hat{x}(1 - (60/62) \ln(\hat{x}))$ term in $M_{\text{eff},2}^{\text{lin}}$.

The reasoning behind the second of these approximations is the following. As argued above, the $\hat{x}(1 - (60/62) \ln(\hat{x}))$ term is important only for large x_{mr} . But in this case, the double-integral contributions to $M_{\text{eff},2}^{\text{lin}}$ are anyway small compared to $M_{\text{eff},2}^{\text{sqrt}}$ so it does not matter. Indeed,

$$\frac{M_{\text{eff},2}^{\text{lin}} - M_{\text{eff},1}}{M_{\text{eff},2}^{\text{sqrt}}} \Big|_{x_{\text{mr}} \gg 1} \approx \frac{31}{25} \frac{1}{x_{\text{mr}}} \frac{(1 + \delta)^2 - 1}{\delta} \hat{x} \left(1 - \frac{60}{62} \ln(\hat{x}) \right), \quad (\text{K.35})$$

where we used $\alpha = 9((1 + \delta)^2 - 1)/x_{\text{mr}}^3$ which is valid for $x_{\text{mr}} \gg 1$, see Eq. (K.11). Since $\hat{x} \leq 1$ and $x_{\text{mr}} \gg 1$, this ratio is small unless $\delta \gtrsim x_{\text{mr}}$. Thus, for our purposes this ratio is small. We are not interested in very large deviations from MOND δ which would be required for $\delta \gtrsim x_{\text{mr}} \gg 1$.

Eq. (K.34) then becomes

$$\frac{-\frac{\alpha \delta}{4} x_{\text{mr}}^3 \hat{x}^4 - \frac{\alpha^2}{8} \hat{x}^4 x_{\text{mr}}^4 \left(1 - \frac{4}{15} \hat{x} \right)}{(1 + \delta \hat{x})^2} \stackrel{!}{=} (1 - q)^2 - 1. \quad (\text{K.36})$$

This is still not solvable analytically. Thus, our final approximation will be to neglect the $-4/15 \hat{x}$ term. This is again a rough approximation but, as mentioned above, we have verified numerically that the result is reasonable. Thus, we need to solve

$$\sqrt{\frac{1}{4} \alpha x_{\text{mr}}^3 \delta + \frac{1}{8} \alpha^2 x_{\text{mr}}^4 \frac{\hat{x}^2}{1 + \delta \hat{x}}} \stackrel{!}{=} \sqrt{1 - (1 - q)^2}. \quad (\text{K.37})$$

We finally find for the radius r_{approx} up to which the 1st order approximation is valid to within a fraction q ,

$$\frac{r_{\text{approx}}}{r_{\text{maxratio}}} = \frac{1}{2} \left(\beta \delta + \sqrt{(\beta \delta)^2 + 4\beta} \right), \quad (\text{K.38})$$

where

$$\beta = \frac{\sqrt{2}}{3} \sqrt{\frac{1 - (1 - q)^2}{\delta^2 (2 + \delta)}} \sqrt{\frac{(3 + 2x_{\text{mr}})^2}{(3 + 2x_{\text{mr}})x_{\text{mr}} + 9(2 + \delta)}}, \quad (\text{K.39})$$

where we used Eq. (K.11) to eliminate α .

Note that we assumed $r \leq r_{\text{maxratio}}$ when deriving this estimate. Thus, if our expression for $r_{\text{approx}}/r_{\text{maxratio}}$ is larger than 1, the 1st order approximation is valid up to at least r_{maxratio} but the precise value of $r_{\text{approx}}/r_{\text{maxratio}}$ is not meaningful.

The most important implication of our estimate is that the 1st order approximation is good for small δ (except for extremely

restrictive values of q). For larger δ , the approximation is worse. Explicitly, for small δ the quantity β scales as

$$\beta_{\delta \ll 1} \sim \sqrt{q}/\delta \quad (\text{K.40})$$

so that $r_{\text{approx}}/r_{\text{maxratio}}$ scales as

$$\left. \frac{r_{\text{approx}}}{r_{\text{maxratio}}} \right|_{\delta \ll 1} \sim \sqrt{\beta} \sim \left(\frac{q}{\delta^2} \right)^{1/4}. \quad (\text{K.41})$$

When δ is small, this ratio is large, so the 1st order approximation is valid. If we demand a better approximation, i.e. a smaller q , the radius r_{approx} becomes smaller.

In the opposite limit, $\delta \gg 1$,

$$\beta_{\delta \gg 1} \sim \sqrt{q/\delta^3} \text{ or } \sqrt{q/\delta^4}, \quad (\text{K.42})$$

where the power 3 applies for sufficiently large x_{mr} and the power 4 for sufficiently small x_{mr} . In both cases does $r_{\text{approx}}/r_{\text{maxratio}}$ tend to zero for large δ . So the 1st order approximation is not valid much.